

Appunti & trasparenze - Parte 10

Versione 3, Dicembre 2004

Francesco Fuso, tel 0502214305, 0502214293 - fuso@df.unipi.it

<http://www.df.unipi.it/~fuso/dida>

Metodi di scansione di sonda per l'osservazione e la realizzazione di nanostrutture: microscopia SPM (STM, AFM, SFM, SNOM) e metodi di nanomanipolazione e nanoscrittura/nanolitografia tramite SPM

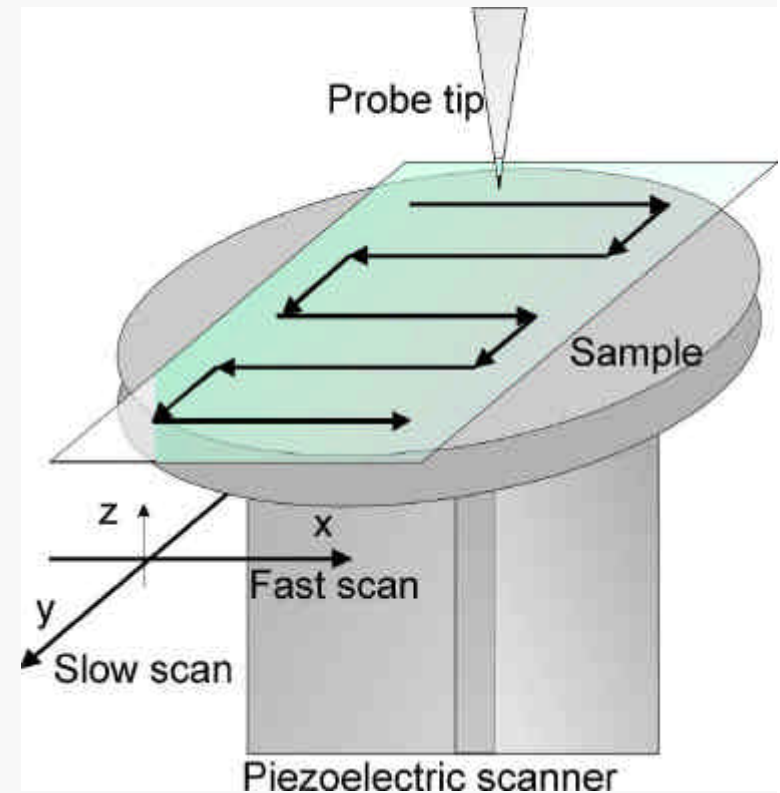
25/11/2004 – 10.30+1 ITI M

Introduzione: Scanning Probe Microscopy (SPM)

Scanning: piezoelectric translator
Probe: tip probing local properties
Microscopy: sub-micrometer resolution
(+ system to control tip/sample distance
+ electronics for instrument operation)

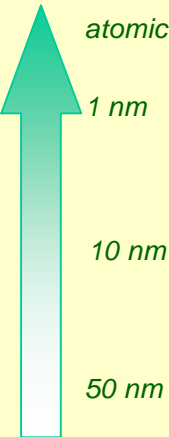
Sviluppato a partire da anni '80 grazie a disponibilità di:

- ✓ Piezoelectric translators con risoluzione sub-nm;
- ✓ Probes di dimensioni sub-nm



Diverse proprietà fisiche locali possono essere misurate punto per punto in una scansione a rastrello ed una (o più) mappe possono essere ricostruite

Alcuni tipi di SPM

Technique	Probed quantity	Resolution
SFM	STM	
	AFM	
	SFFM	
	MFM	
	EFM	
	SNOM	
	Ap-SNOM	
...	...	

Possono essere realizzati numerosi “tipi” di SPM in funzione del tipo di sonda e della proprietà fisica sondata

Piezoelectric scanner

...the coefficient d is negative representing contraction perpendicular to the field; and positive for strain measured along the 3-direction (along which the thickness t is measured) representing expansion parallel to the electric field direction:

$$\Delta t = d_{33} V. \quad (4.4)$$

Although there are many ceramic compositions used today, most can be placed into two general categories: hard and soft PZT materials. Typical d coefficients for hard PZT materials are

$$d_{33} = 250 \cdot 10^{-12} \text{ m/V}, \quad d_{31} = -110 \cdot 10^{-12} \text{ m/V};$$

and for soft PZT materials

$$d_{33} = 600 \cdot 10^{-12} \text{ m/V}, \quad d_{31} = -270 \cdot 10^{-12} \text{ m/V}.$$

For PZT-5H

$$d_{33} = 593 \cdot 10^{-12} \text{ m/V}, \quad d_{31} = -273 \cdot 10^{-12} \text{ m/V}.$$

Tipicamente, tubi cavi con elettrodi disposti in modo da provocare spostamenti nelle tre direzioni.

Problemi:

- Linearità (eventuale closed loop);
- Isteresi (controllabile via software);
- Distorsioni geometriche ed artefatti.

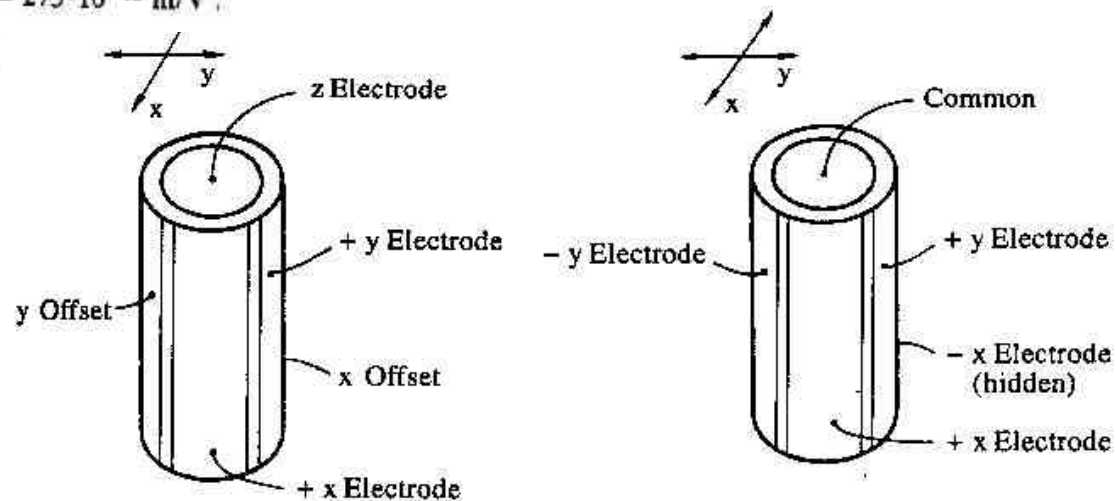


Fig. 4.5. Illustrating the voltages applied to the electrodes of the single-tube scanner

Scanning Tunneling Microscope (STM) I

2.1 Theoretical Fundamentals of the Scanning Tunneling Microscope

How does a measuring instrument function that allows us to see single atoms? In the case of a scanning tunnelling microscope a fine metallic tip is used as the probe (called tunnelling tip) (see Figure 3). This tip is approached toward the surface until a current flows when a voltage is applied between the tip and the sample surface. This happens at distances in the order of 1 nm. The current is called tunnel current since it is based on the quantum-mechanical tunnel effect. After a tunnelling contact is established, the tip is moved over the surface by a piezoelectric scanning unit, whose mechanical extension can be controlled by applying appropriate voltages. The scanning unit is typically capable of scanning an area of a few nm up to several μm . This allows us to obtain a microscopic image of the spatial variation of the tunnel current. Hence the name scanning tunnelling microscope.

- A metallic tip is moved as probe towards a conducting surface up to a distance of about 1 nm
- With an applied voltage a current flows due to the tunnel effect (tunnel current)
- The spatial variation of the tunnel current is measured by scanning over the sample surface
- A microscopic image of the surface is produced

At this stage we have to ask what kind of atomic-scale structures can be made visible by the scanning tunnelling microscope utilising the tunnel effect? These structures must by nature correspond to electrical states from or into which the electrons can tunnel. In the tunnelling process, the electrons must tunnel through the vacuum barrier between tunnelling tip and sample, which represents a potential barrier. The tunnel effect allows a particle (here an electron) to tunnel through this potential barrier even though the electron's energy is lower than the barrier height. The probability of such a process decreases exponentially with the geometrical distance between the tip and the sample and with increasing barrier height. An experimental apparatus making use of the tunnel effect must therefore minimise the potential barrier to be tunnelled through. This is realised in the scanning tunnelling microscope configuration by moving the tip very close (about 1 nm) to the surface. The electrons can then pass between the surface and the tip. The direction of the tunnel current is fixed by applying a voltage between sample and tip.

In order to explain and interpret the images of the surface states obtained in this way, efforts to develop a theory were made very soon after the invention of the scanning tunnelling microscope. One of the possible theoretical approaches is based on Bardeen's idea of applying a transfer Hamiltonian operator to the tunnelling process [2]. This had the advantage of adequately describing the many-particle nature of the tunnel junction. In the model, a weak overlap of the wave functions of the surface states of the two electrodes (tunnelling tip and sample surface) is assumed to allow a perturbation calculation. On this basis, Tersoff and Hamann developed a simple theory of scanning tunnelling microscopy [3], [4]. Hence follows the tunnel current:

$$I \sim V \cdot \rho_{\text{tip}}(W_F) \cdot \rho_{\text{sample}}(W_F) \quad (1)$$

The tunnelling tip is assumed to be a metallic s-orbital as shown schematically in Figure 4. In addition, it is assumed that low voltages V (i.e., much smaller than the work function) are applied. $\rho_{\text{tip}}(W_F)$ is the density of states of the tip and $\rho_{\text{sample}}(W_F)$ is that of the sample surface at the centre r_s of the tip orbital and at the Fermi energy W_F . Eq. (1) shows that at low voltage the scanning tunnelling microscope thus images the electronic density of states at the sample surface near the Fermi energy. However, this result also means that the scanning tunnelling microscope images do not directly show the atoms, but rather the electronic states bound to the atoms. As can be seen in Eq. (1), the tip's density of states enters in the measurement in the same way as the density of states of the sample. It is therefore desirable to know the exact electronic state of the tip, but unfortunately, in practice, every tip is different and the details remain unknown.

- Weak overlap of the wave functions of the surface states of the two electrodes (tunnelling tip and sample surface)
- Tunnelling tip approximated as an s-orbital
- Low voltages ($V \ll$ work function)

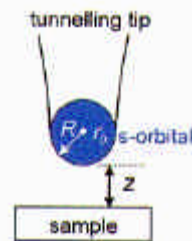
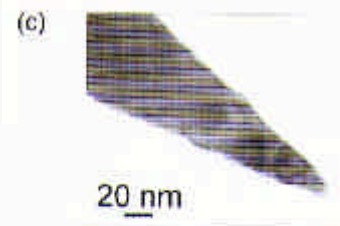
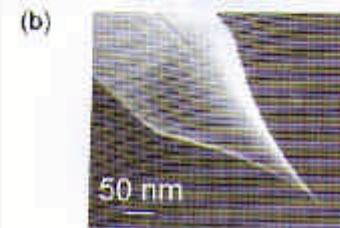
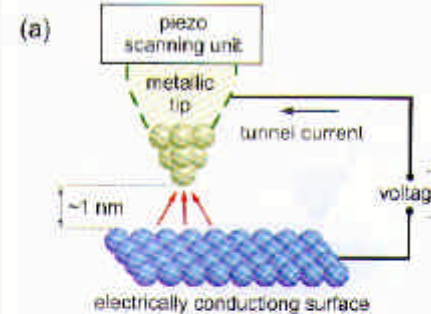


Figure 4: Schematic representation of the tunnelling geometry in the Tersoff-Hamann model.

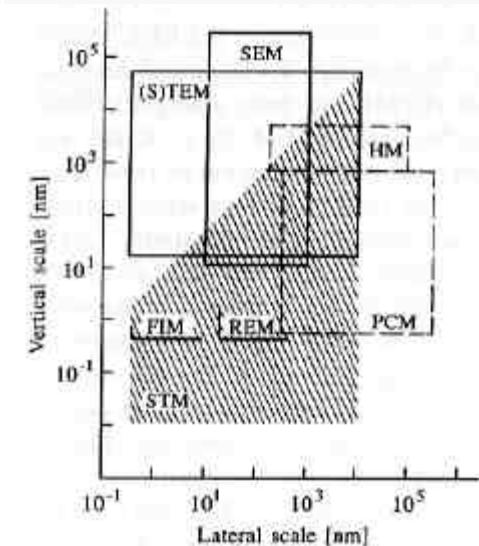


Fig. 1.1. Comparison of the resolution range of STM with that of other microscopes [1.1]. [HM: High-resolution optical Microscope, PCM: Phase Contrast Microscope, (S)TEM: (Scanning) Transmission Electron Microscope, FIM: Field Ion Microscope, REM: Reflection Electron Microscope]

STM raccoglie informazioni locali sulla densità degli stati superficiali in prossimità del livello di Fermi

Figure 3:

(a) Schematic representation of the scanning tunnelling microscope: the tunnel current is used as measurement signal. (b) and (c) show a scanning and transmission electron microscope image, respectively, of a typical metallic tip used for a scanning tunnelling microscope.

Scanning Tunneling Microscope (STM) II

- The tunnel current is proportional to the local density of states of the sample
- The scanning tunneling microscope images the electronic local density of states of the sample near the Fermi energy.

In a first approximation the density of surface states decreases exponentially into the vacuum with the effective inverse decay length k_{eff}

$$k_{eff} = \sqrt{\frac{2m_e B}{\hbar^2} + |k_{||}|^2} \quad (2)$$

m_e is the electron mass and $k_{||}$ is the parallel wave vector of the tunnelling electrons. B is the barrier height, which is approximately a function of the applied voltage V and the work functions Φ_{sample} and Φ_{tip} of the sample and tip [5], respectively:

$$B = \frac{\Phi_{tip} + \Phi_{sample}}{2} - \frac{|eV|}{2} \quad (3)$$

The tunnel current thus decreases exponentially with the tip-sample distance z :

$$I \sim \exp[-2k_{eff}z] \quad (4)$$

The exponential current-voltage dependence is quite essential for the high measurement accuracy of a scanning tunneling microscope, since even small changes in distance may cause a large change in the tunnel current. Thus the tip just needs one microtip, which is only about 0.1 nm closer to the surface than the next one, and still all current flows over only the closest microtip. Thus even apparently wide tips can yield atomic resolution via one microtip.

The description of the tunnel current by Eq. (1) however, has an important restriction: it strictly speaking only applies to low voltages V . In particular for the investigation of semiconductor surfaces voltages of the order of 2 to 3 V are required due to the existence of a band gap. Thus the theory must be extended. The simplest extension yields:

$$I \sim \int_{W_{F,tip}}^{W_{F,tip}+eV} \rho_{tip}(W) \rho_{sample}(W+eV) T(W,V) dW \quad (5)$$

$T(W,V)$ is a transmission coefficient which depends on the energy of the electrons and the applied voltage. The tunnel current is composed of the product of the density of states of the tip and sample at all the different electron energies that are allowed to participate in the tunnelling process (Figure 5). For example, an image measured at -2 V applied to the sample, consequently shows all occupied sample states with an energy between the Fermi energy and 2 eV below the Fermi energy. Tunnelling at a positive voltage analogously provides a measurement of the empty surface states in an energy interval determined again by the voltage.

In order to illustrate this effect more clearly, in the following the InP(110) surface will be presented. On InP(110) surfaces two electrical states exist near the surface: an occupied state below the valence band edge and an empty state above the conduction band edge (Figure 6). All the other states are located geometrically deeper in the crystal or energetically deeper in the bands. They thus contribute little to the tunnel current.

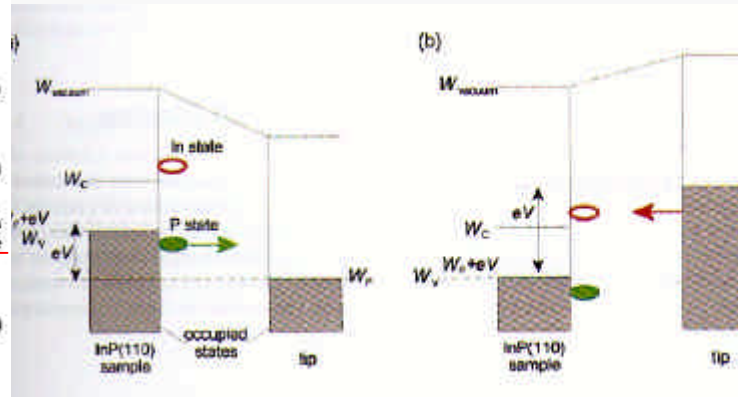


Figure 6: Schematic of the tunnelling process at (a) negative and (b) positive voltages applied to the InP(110) surface.

Extension to "high" voltages

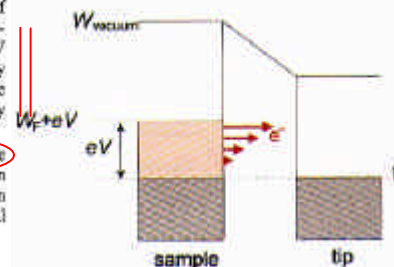


Figure 5: At high voltages not only the states near the Fermi energy W_F contribute to the current but all states whose energy ranges between W_F and $W_F + eV$.

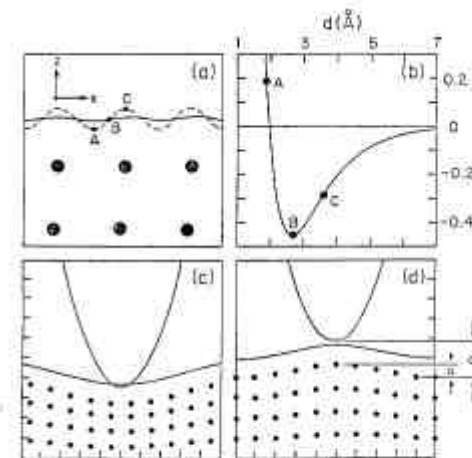


Fig. 2.15: (a) Contour plot of constant local density of states (dashed line) and contour of total charge density (solid line). Filled circles indicate the positions of carbon atoms of the top two layers. (b) Potential used for the interaction of tip and surface (schematic). (c) Compression and (d) expansion of graphite for the tip at points A and C of (a), respectively [2, 13].

Da R. Waser Ed., Nanoelectronics and information technology (Wiley-VCH, 2003)

Scanning Tunneling Microscope (STM) III

In the special case of the $\text{InP}(110)$ surface, the occupied surface state is spatially located above the P atoms, whereas the empty state is bound to the In atoms (Figure 7a,b). The P and In atoms are alternately arranged in zigzag rows. At negative sample voltages, the scanning tunnelling microscope probes the occupied states located at the P sublattice, whose electrons tunnel into the empty states of the tunnelling tip (Figure 6a). Conversely, only the empty surface states at the In sublattice are probed at positive voltages applied to the sample (Figure 6b) [6] - [8]. If the voltage polarity is changed every scan line, i.e. the occupied and the empty states are probed each alternating scan line, the two resulting images can be superimposed and the zigzag rows of alternating "In" and "P" atoms become visible (Figure 7c).

Apart from the spatial distribution of the density of states, its energy dependence is also of interest, and it should be possible to determine this dependence from current-voltage characteristics using Eq. (5). In order to do so, however, information is required about the transmission coefficient, which turns out to be a great obstacle even if approximations [9] are used. Therefore, in most cases, an experimentally viable approach is used, in which the density of states is approximated as follows [10], [11]:

$$\rho_{\text{sample}}(eV) \approx (dI/dV)/(eV) \quad (6)$$

It is thus possible to experimentally measure the density of states as a function of the energy relative to the Fermi level.

"Spettroscopia" STM

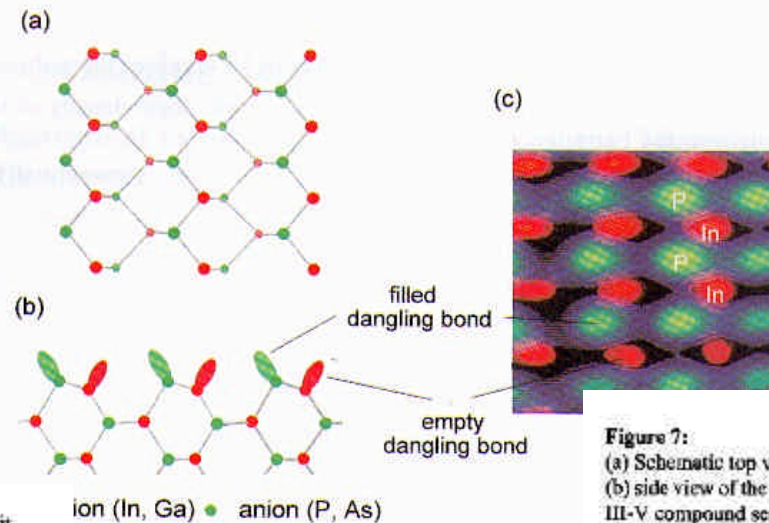


Figure 7:
(a) Schematic top view and (b) side view of the (110) surfaces of III-V compound semiconductors. (c) Superposition of two scanning tunnelling microscope images measured at positive (red) and negative (green) voltage. The density of state maxima correspond to the surface states at the In and P atoms, respectively.

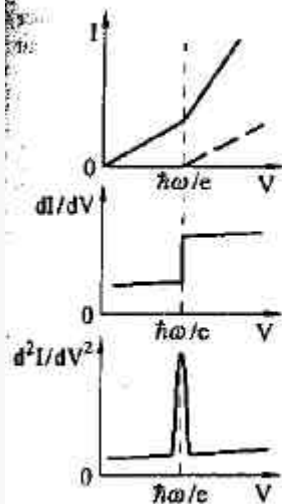


Fig. 3.1. The current versus voltage curve has a kink in it when the inelastic electron tunneling channel opens up. This kink becomes a step in the first derivative and a peak in the second derivative.

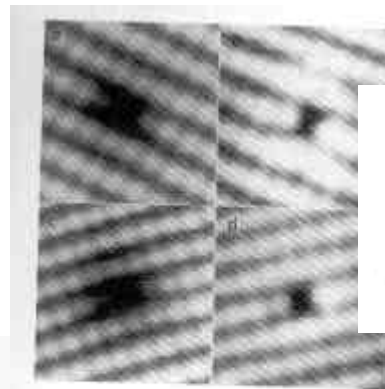
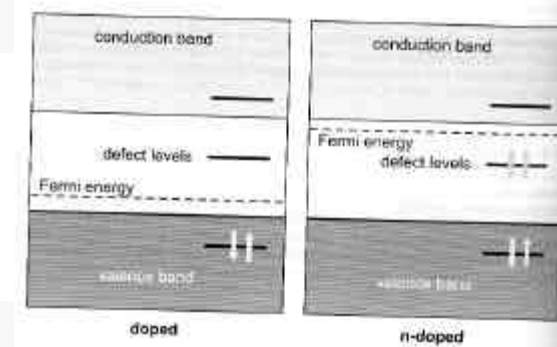


Figure 11: Phosphorus vacancies on (a) p- and (b) n-doped GaP(110) and (c) p- and (d) n-doped InP(110). On the left, two positively charged vacancies are shown, whereas on the right they are negatively charged.

Figure 12: Schematic of the electron population of the defect energy level on p- and n-doped InP(110) and GaP(110) surfaces. On the left the vacancy is positively and on the right negatively charged.



Preparazione tips STM ed artefatti topografici

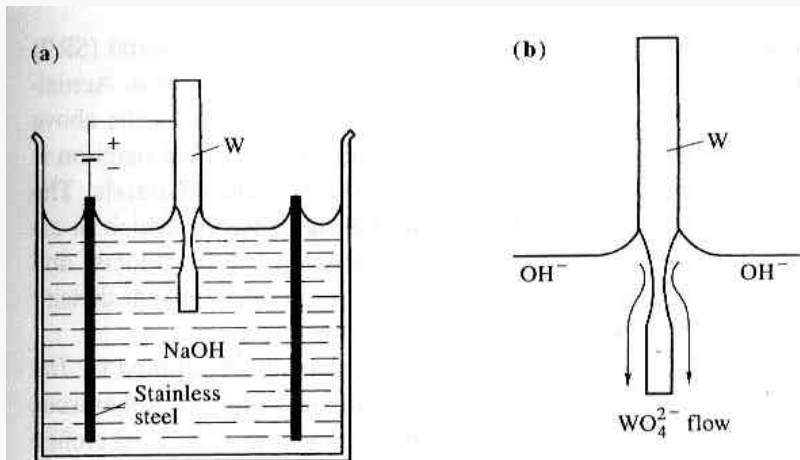
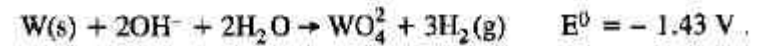
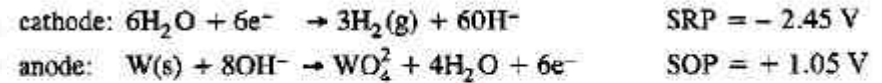


Fig. 4.12. (a) Schematic diagram of the electrochemical cell showing the tungsten wire (anode) being etched in NaOH. The cathode consists of a stainless-steel cylinder which surrounds the anode. (b) Sketch of the etching mechanism showing the "flow" of the tungstate anion down the sides of wire in solution [4.13]



Tipicamente, le tips sono fili metallici appuntiti tramite etching elettrochimico

La geometria della tip può facilmente indurre artefatti topografici

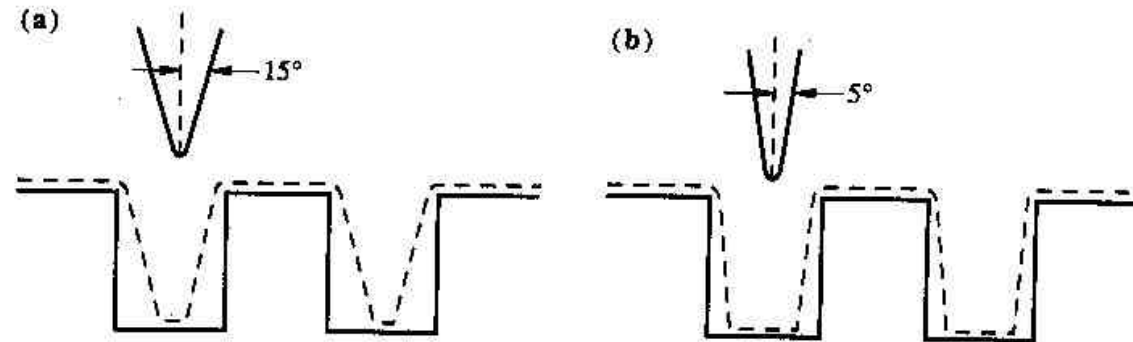


Fig. 4.15a,b. Effect of tip geometry on the measured STM profile of grooves $0.75 \mu\text{m}$ wide and $1 \mu\text{m}$ deep using: (a) a tip with a 50 nm radius of curvature and 15° cone half angle, (b) a tip with a 50 nm radius of curvature and 5° cone half angle

Modi di operazione dell'STM

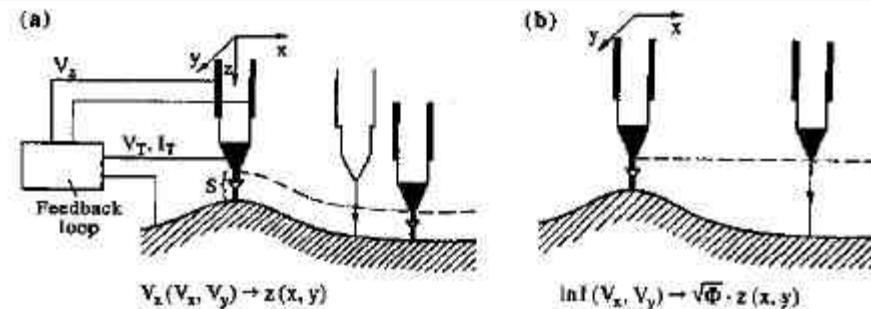
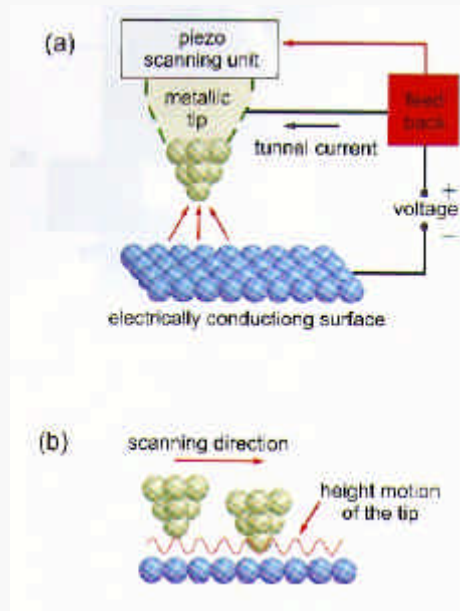


Fig. 1.2a,b. Schematic view of two modes of operation in STM [1.10]. S is the gap between the tip and the sample. I and V_T are the tunneling current and bias voltage, respectively, and V_z is the feedback voltage controlling the tip height along the z direction. (a) constant-current mode and (b) constant-height mode

2.2 Operating Modes of the Scanning Tunneling Microscope

Up to now, the theoretical background of a scanning tunnelling microscope has been presented, but nothing has been said about the experimental operation of a scanning tunnelling microscope. The simplest way to obtain a scanning tunnelling microscope image is to directly measure the variation of the tunnel current as a function of the scanning position while keeping the distance between tip and sample surface constant. A so-called current image is then obtained. Instead of directly recording the atomic variation of the current, however, the usual procedure is to keep the tunnel current constant while scanning over the surface. This is done by changing the distance between tip and surface using a feedback loop (Figure 8). In order to get an image, the voltage required at the piezoelectric crystal to adjust the distance is recorded. One obtains a so-called constant-current STM image.

Feedback loop necessario per mantenere costante la corrente di tunnel

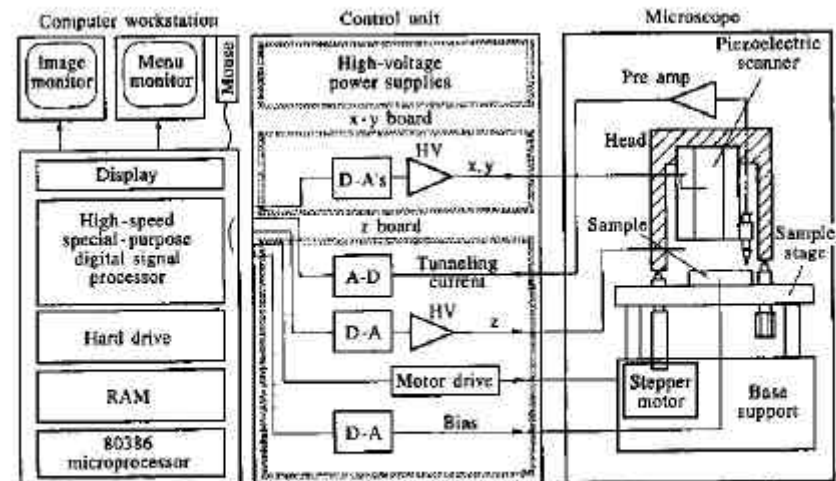


Fig. 4.27. Block diagram of the STM control, data acquisition and display system indicating all of the equipment connections

Vantaggi e limiti dell'STM

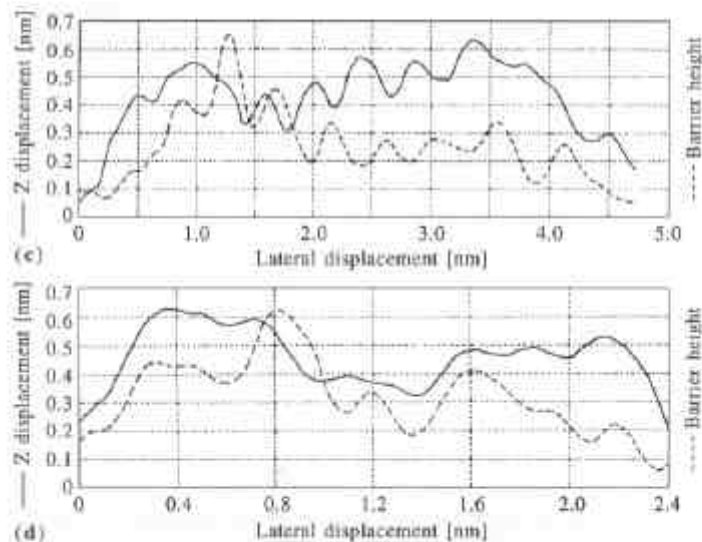
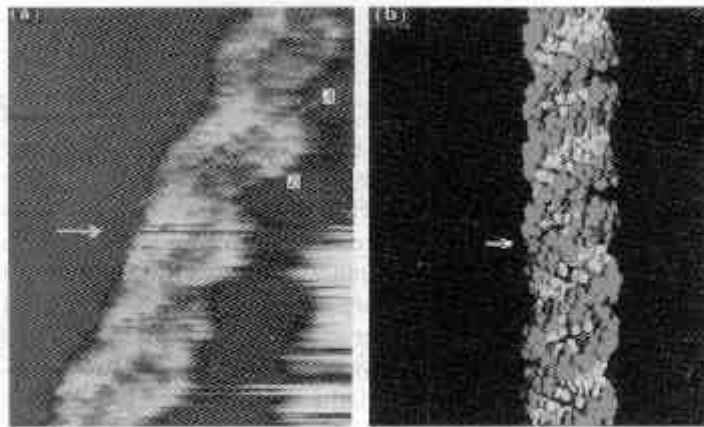


Fig. 8.5a-d. An STM image of A-DNA in vacuum [8.18]. (a) Unsmoothed, unfiltered plane-subtracted STM image of A-DNA ($8 \times 12 \text{ nm}^2$). (b) A-DNA model based on X-ray diffraction results. (c) *Solid line*: interpolated cross section following line marked A on Fig. 8.5a; *dashed line*: corresponding data from a simultaneously acquired gap-modulated barrier-height image. (d) *Solid line*: interpolated cross section following line marked B on Fig. 8.5a; *dashed line*: corresponding data from a simultaneously acquired barrier-height image.

Possibilità di risolvere spazialmente la distribuzione elettronica legata a differenti atomi, cioè di “vedere” gli atomi

Virtualmente, nessuna necessità di preparazione campioni e possibilità di operare in aria

Non si applica facilmente a materiali con scarse proprietà di conduzione

Esempio di applicazione a campioni biologici

Scanning Force Microscope (SFM) I

3.1 Theoretical Principles of the Scanning Force Microscope

As already mentioned above, van der Waals forces lead to an attractive interaction between the tip on the spring and the sample surface. Figure 15 shows schematically the van der Waals potential between two atoms. The potential can be described in a simpler classical picture as the interaction potential between the time dependent dipole moments of the two atoms. Although the centres of gravity of the electronic charge density and the charge of nucleus are exactly overlapping on a time average, the separation of the centres of gravity is spatially fluctuating in every moment. This produces statistical fluctuations of the atoms' dipole moments. The dipole moment of an atom can again induce a dipole moment in the neighbouring atom and the induced dipole moment acts back on the first atom. This creates a dipole-dipole interaction on basis of the fluctuating dipole moments. This interaction decreases with d^6 in the case of small distances d (Lenard-Jones potential). At larger distances, the interaction potential decreases more rapidly (d^3). This arises from the fact that the interaction between dipole moments occurs through the exchange of virtual photons. If the transit time of the virtual photon between atoms 1 and 2 is longer than the typical fluctuation time of the instantaneous dipole moment, the virtual photon weakens the interaction. This range of the van der Waals interaction is therefore called retarded, whereas that at short distances is unretarded.

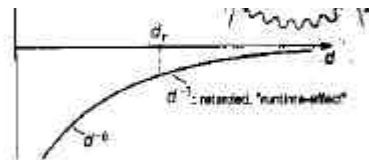


Figure 15: The van der Waals potential U between two atoms. d_c is the critical distance above which the transit time effects weaken the interaction [23].

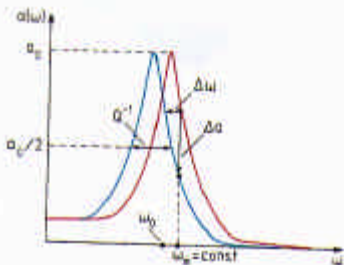


Figure 17: Resonance curves of the tip without and with interaction with a van der Waals potential. The interaction leads to a shift $\Delta\omega$ of the resonance frequency with the consequence that the tip excited with the frequency ω_0 has a vibration amplitude $a(\omega)$ attenuated by Δa [23].

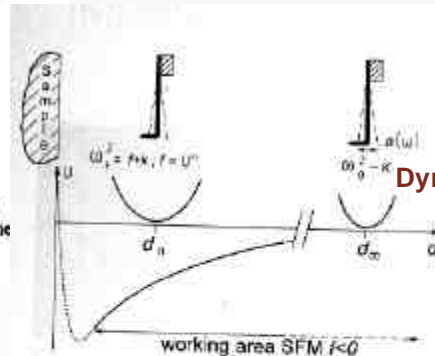


Figure 16: Schematic representation of the effect of the van der Waals interaction potential on the vibration frequency of the spring with tip. As the tip approaches the surface, the resonance frequency of the leaf spring is shifted. (from [23]).

The scanning force microscope is not based on the interaction of individual atoms only. Both the sample and the tip are large in comparison to the distance. In order to obtain their interaction, all forces between the atoms of both bodies need to be integrated. The result of this is known for simple bodies and geometries. In all cases, the summation leads to a weaker decrease of the interaction. A single atom at distance d relative to a half-space leads to an interaction potential of

$$U = -\frac{C\pi\rho}{6} \cdot \frac{1}{d^3} \quad (7)$$

where C is the interaction constant of the van der Waals potential and ρ the density of the solid. C is basically determined by the electronic polarizabilities of the atoms in the half-space and of the single atom. If one has two spheres with radii R_1 and R_2 at distance d (distance between sphere surfaces) one obtains an interaction potential of

$$U = -\frac{AR_1R_2}{6(R_1 + R_2)} \cdot \frac{1}{d} \quad (8)$$

where A is the so-called Hamaker constant. It is materials specific and essentially contains the densities of the two bodies and the interaction constant C of the van der Waals potential. If a sphere with radius R has a distance d from a half-space, an interaction potential of

$$U = -\frac{AR}{6} \cdot \frac{1}{d} \quad (9)$$

is obtained from Eq. (8). This case describes the geometry in a scanning force microscope best and is most widely used. The distance dependence of the van der Waals potential thus obtained is used analogously to the distance dependence of the tunnel current in a scanning tunnelling microscope to achieve a high resolution of the scanning force microscope. However, since the distance dependence is much weaker, the sensitivity of the scanning force microscope is lower.

The dynamic operation method of a scanning force microscope has proved to be particularly useful. In this method the nominal force constant of the van der Waals potential, i.e. the second derivative of the potential, is exploited. This can be measured by using a vibrating tip (Figure 16). If a tip vibrates at distance d , which is outside the interaction range of the van der Waals potential, then the vibration frequency and the amplitude are only determined by the spring constant k of the spring. This corresponds to a harmonic potential. When the tip comes into the interaction range of the van der Waals potential, the harmonic potential and the interaction potential are superimposed thus changing the vibration frequency and the amplitude of the spring.

This is described by modifying the spring constant k of the spring by an additional contribution f of the van der Waals potential. As a consequence, the vibration frequency is shifted to lower frequencies as shown in Figure 17. ω_0 is the resonance frequency without interaction and $\Delta\omega$ the frequency shift to lower values. If an excitation frequency of the tip of $\omega_{ex} > \omega_0$ is selected and kept constant, the amplitude of the vibration decreases as the tip approaches the sample, since the interaction becomes increasingly stronger. Thus, the vibration amplitude also becomes a measure for the distance of the tip from the sample surface. If a spring with low damping Q^{-1} is selected, the resonance curve is steep and the ratio of the amplitude change for a given frequency shift becomes large.

In practice, small amplitudes (approx. 1 nm) in comparison to distance d are used to ensure the linearity of the amplitude signal. With a given measurement accuracy of 1%, however, this means that the assembly must measure deflection changes of 0.01 nm, which is achieved most simply by a laser interferometer or optical lever method.

Scanning Force Microscope (SFM) II

3.2 The Operation Principle of Scanning Force Microscope

The main electronic components of the SFM are the same as for the STM, only the topography of the scanned surface is reconstructed by analysing the deflection of the tip at the end of a spring. Today, the interferometrical and optical lever method dominate commercial SFM apparatus. The most common method for detecting the deflection of cantilever is by measuring the position of a reflected laser-beam on a photosensitive detector. The principle of this optical lever method is presented in Figure 18 a. Without

cantilever displacement both quadrants of the photodiode (A and B) have the same irradiation $P_A = P_B = P/2$ (P represents the total light intensity). The change of the irradiated area in the quadrants A and B is a linear function of the displacement

$$\delta \propto \Delta d = 2 \sin(\Theta) \cdot S_2 = 2\Theta \cdot S_2 = 3S_2 \cdot \delta/L \quad (10)$$

For small angles $\sin(\Theta) \approx \Theta$ and Θ may be evaluated from the relation $\Theta = 3\delta/2L$ (Figure 18b). For P_A and P_B one would get approximately $P_A = P/2 \cdot (d + \Delta d)/2$ and $P_B = P/2 \cdot (d - \Delta d)/2$. Using the simple difference between P_A and P_B would lead to

$\Delta P = P \cdot 3S_2/(Ld)$ but in this case one cannot distinguish between the displacement δ of the cantilever and the variation in the laser power P . Hence the normalised difference is used, which is only dependent of δ :

$$\frac{P_A - P_B}{P_A + P_B} = \delta \cdot \frac{3S_2}{Ld} \quad (11)$$

The "lever amplification" $\Delta d/\delta = 3S_2/L$ is about a factor of one thousand. On the basis of this kind of technique one is able to detect changes in the position of a cantilever of the order of 0.01 nm.

For large distances between the tip and the sample the bending of the cantilever by attractive forces is negligible. After the cantilever is brought closer to the surface of the sample (point "a" Figure 18c) the van der Waals forces induce a strong deflection of the cantilever and, simultaneously, the cantilever is moving towards the surface. This increases the forces on the cantilever, which is a kind of positive feedback and brings the cantilever to a direct contact with the sample surface (point "b"). However, when the cantilever is brought even closer in contact to the sample, it actually begins to bend in the opposite direction as a result of a repulsive interaction ("b-c"). In the range ("b-c") the position of the laser beam on both quadrants, which is proportional to the force, is a linear function of distance. On reversal this characteristic shows a hysteresis. This means that the cantilever loses contact with the surface at a distance (point "d") which is much larger than the distance on approaching the surface (point "a").

Up to now, the actual probe, i.e. the tip of the leaf spring, has not been discussed in detail. Its preparation is particularly demanding since the tip and the sensitive spring should be one piece. Moreover, the cantilever should be as small as possible. Nowadays, such scanning tips are commercially available (in contrast to the tunnelling tips, which you should prepare yourself). Figure 19 shows such a spring with tip (cantilever) made of Si. The characteristic parameters of a cantilever has been presented in Figure 18b. The spring constant $k = Ead^3/4L^3 \sim 0.1 - 10 \text{ N/m}$ of the cantilever enables topographical analysis with atomic resolution.

For the realisation of a scanning force microscope, the force measurement must be supplemented by a feedback control, in analogy to the scanning tunnelling microscope. The controller keeps the amplitude of the vibration of the cantilever (the tip), and thus also the distance, constant. During scanning the feedback controller retracts the sample with the scanner of a piezoelectric ceramic or shifts towards the cantilever until the vibration amplitude has reached the setpoint value again. The principle of height regulation is exactly the same as for the scanning tunnelling microscope. The scanning force micrographs thus show areas of constant effective force constant. If the surface is chemically homogeneous and if only van der Waals forces act on the tip, the SFM image shows the topography of the surface.

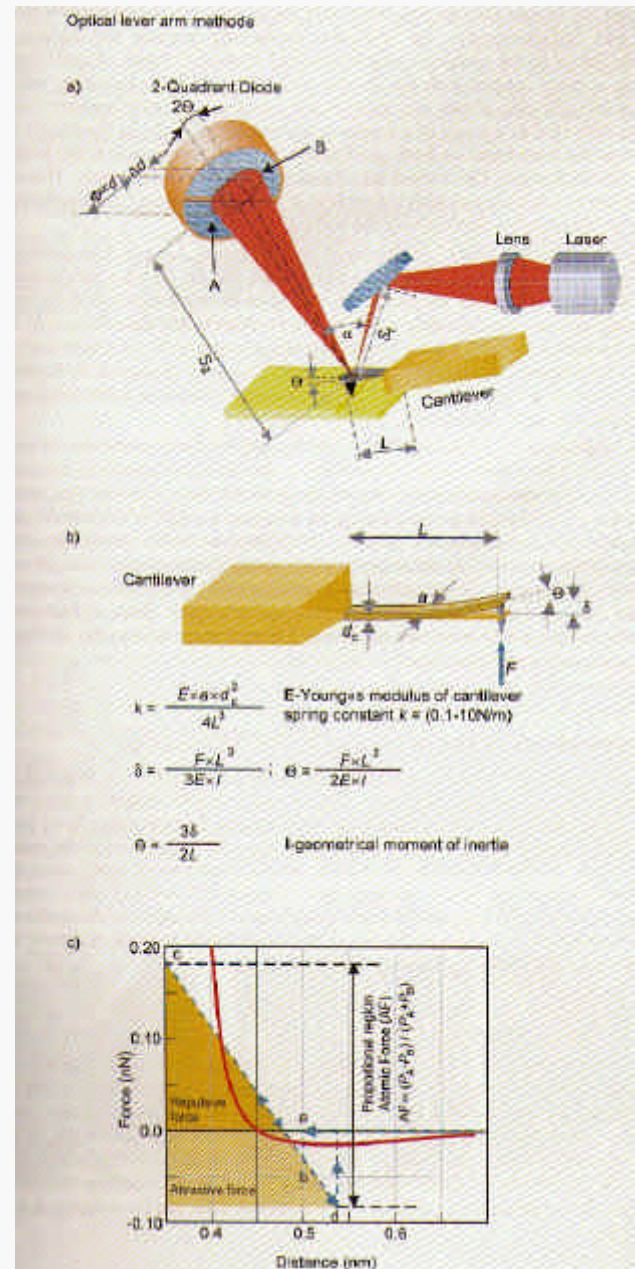


Figure 18: The amplification of the cantilever motion through the optical lever arm method.

(a) Optical laser path in the standard AFM set-up.
(b) Cantilever beam in bending.
(c) Cantilever force as a function of the distance tip – sample distance.

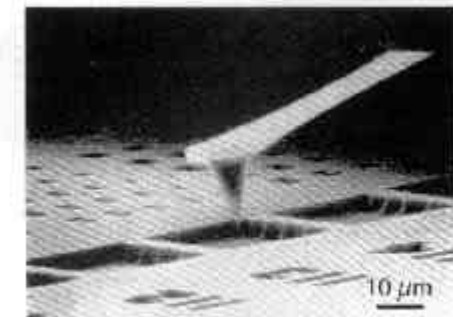


Figure 19: Scanning electron micrograph of a cantilever made of Si. [24]

Cantilevers per SFM (AFM)

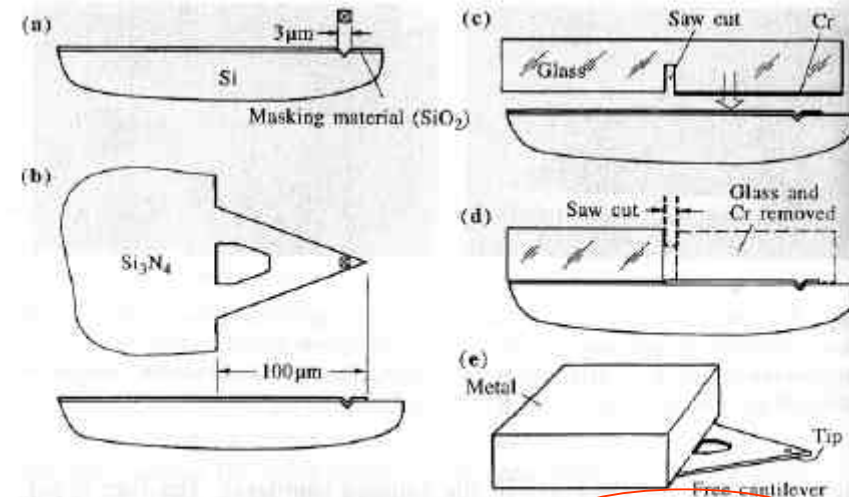
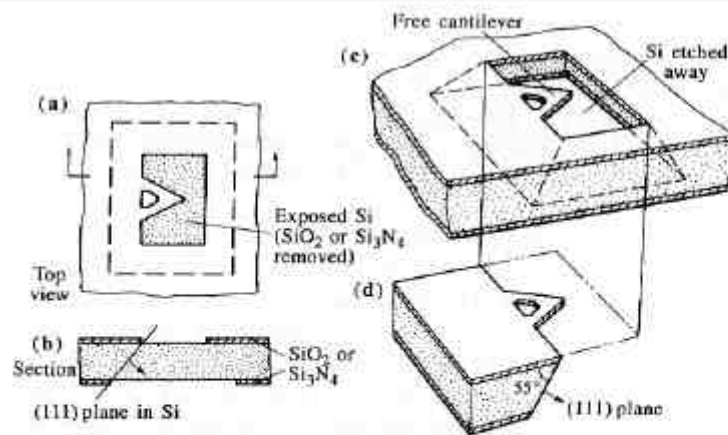


Fig. 5.4a-e. Fabrication of Si_3N_4 microcantilevers with integrated pyramidal tips (a) to (e) illustrate the steps in the fabrication process, see text [5, 4]

Metodi avanzati di microfabbricazione necessari per realizzare tips integrate su microcantilevers

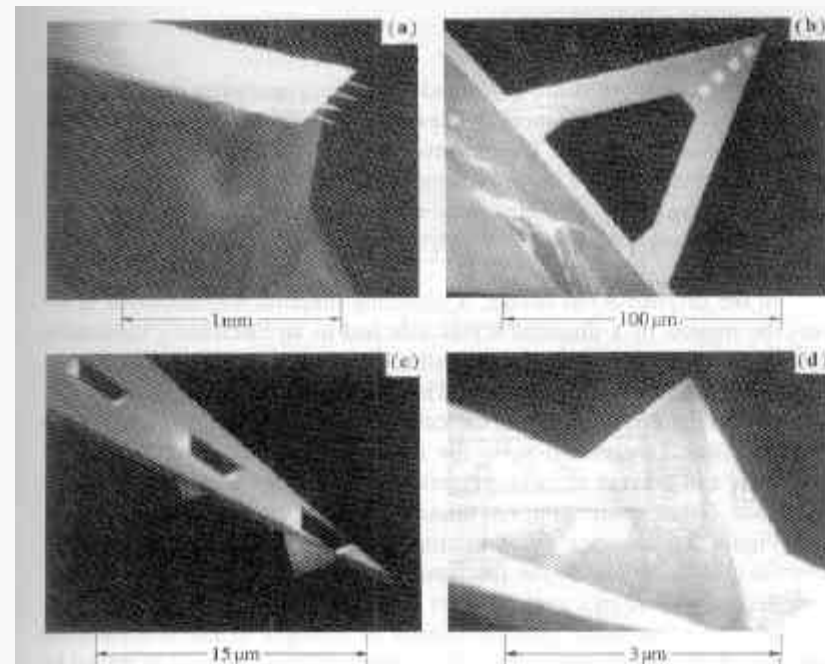


Fig. 5.5a-d. SEM micrographs of Si_3N_4 cantilevers with integrated pyramidal tips. (a) The Si_3N_4 film is attached to the surface of a glass block with dimensions of $2 \times 3 \times 0.7 \text{ mm}^3$. Four cantilevers protrude from the edge of the block. (b) Four pyramidal tips can be seen at the end of this V-shaped cantilever. (c) The pyramidal tips are hollow when viewed from the back side. (d) Each tip has very smooth sidewalls, and the tip appears to terminate virtually at a point, with less than 30 nm radius [5, 4]

Cantilevers commerciali (esempi)

Microlevers™

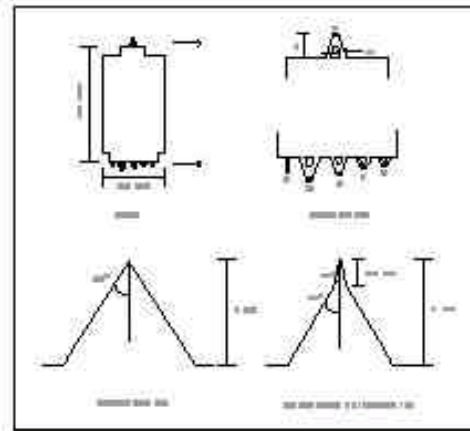
GENERAL PURPOSE CANTILEVERS

FEATURES:

- Compatible with all major AFM brands.
- Typical radius of curvature: sharpened tips: < 20 nm, unsharpened tips: < 50 nm.
- Available with gold coating for high reflectivity.
- Recessed corners for easy sample approach.
- The widest range of spring constants commercially available on a single chip.



Thermomicroscopes Microlevers are ideal for all contact imaging modes, force modulation microscopy, and liquid operation. The range in force constants enable users to image soft samples in contact as well as high load force vs. distance spectroscopy.



Typical Mechanical Characteristics

Cantilever Type	A - triangular	B - rectangular	C - triangular	D - triangular	E - triangular	F - triangular
Standard mode of operation	Contact					
Cantilever length	180 µm	200 µm	170 µm	220 µm	140 µm	85 µm
Cantilever width	18 µm	30 µm	22 µm	22 µm	18 µm	18 µm
Cantilever thickness	0.6 µm	0.6 µm	0.6 µm	0.6 µm	0.6 µm	0.6 µm
Force Constant	0.05 N/m	0.02 N/m	0.01 N/m	0.03 N/m	0.10 N/m	0.50 N/m
Resonant Frequency	22 kHz	13 kHz	7 kHz	15 kHz	38 kHz	120 kHz

Ordering Information

Microlevers	Sharpened		Unsharpened	
	Gold coated*	Uncoated	Gold coated*	Uncoated
Half wafer - (250 chips)	MSCT-AURW	MSCT-NCHW	MLCT-AURW	MLCT-NCHW
Uncoated - (25 chips)	MSCT-AUNM	MSCT-NONM	MLCT-AUNM	MLCT-NONM
Mounted - (25 chips)	MSCT-AUMT-A	MSCT-NOMT-A	MLCT-AUMT-A	MLCT-NOMT-A
Mounted - (25 chips)	MSCT-AUMT-BF	MSCT-NOMT-BF	MLCT-AUMT-BF	MLCT-NOMT-BF

* Not for use with AutoProbe MP systems

ThermoMicroscopes
AFM/SPM/STM/MTM/MTM/MTM

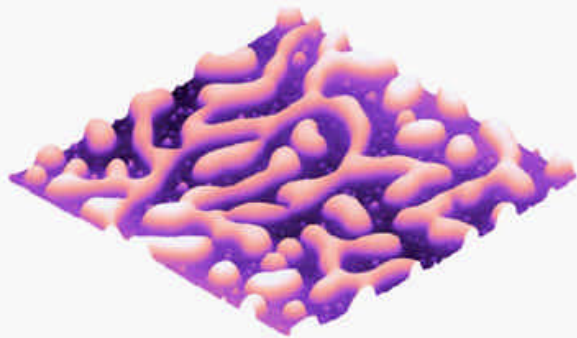
To Place an order, contact:

ThermoMicroscopes
1171 Bonanza Avenue, Sunnyvale, CA 94089
Tel: (415) 747-1800 Fax: (415) 747-1801
E-mail: info@thermomicro.com
Web: www.thermomicro.com
Online Ordering: www.spmimaging.com

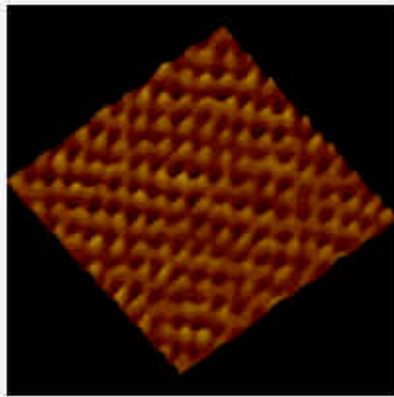
Grande disponibilità di cantilevers di diversi materiali (eventualmente ricoperte di metalli), con diverse geometrie e costanti elastiche

Possibilità di operare SFM "in contatto" (senza modulazione veloce della posizione della cantilever) o "in non contatto" (es., in *tapping mode*) usando cantilevers con costanti elastiche adeguate

Qualche esempio di AFM

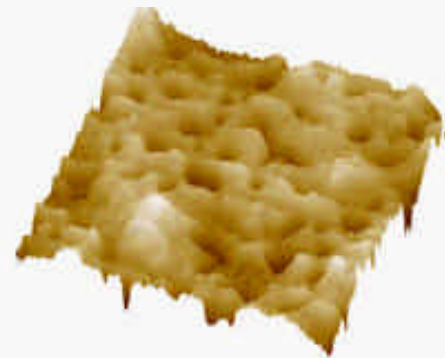
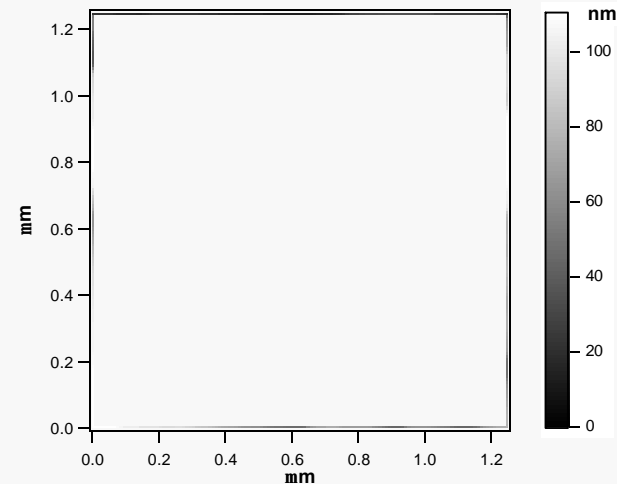


TappingMode AFM image of poly(styrene) and poly(methyl methacrylate) blend polymer film. The film was spin-cast on mica substrate from chloroform solution. The surface structure is resulted from the spinodal decomposition. The islands consist of a PMMS-rich phase while the surface matrix composes of a PS-rich phase. 3 μ m scan courtesy C. Ton-That, Robert Gordon University, U.K.



Atomic-resolution image of the titanium oxide layer on top of a titanium substrate. Contact mode AFM in air, commercial silicon nitride cantilever. 5 nm scan courtesy P. Cacciafesta, University of Bristol, UK.

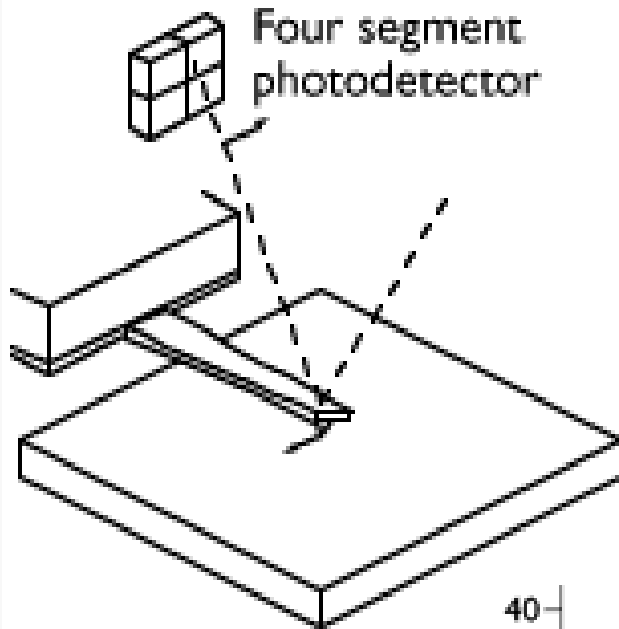
See <http://www.veeco.com>



The sample is a strip of adhesive (3M Scotch tape) that has been peeled of a metal surface. The image shows small pits in the sticky surfaces of the adhesive. The image was acquired in TappingMode at frequency of 3 Hz and setpoint of 1.8 V. 2 μ m scan courtesy L. Scudiero, Washington State University, USA.

Microscopia a forza laterale (LFM, SFFM) I

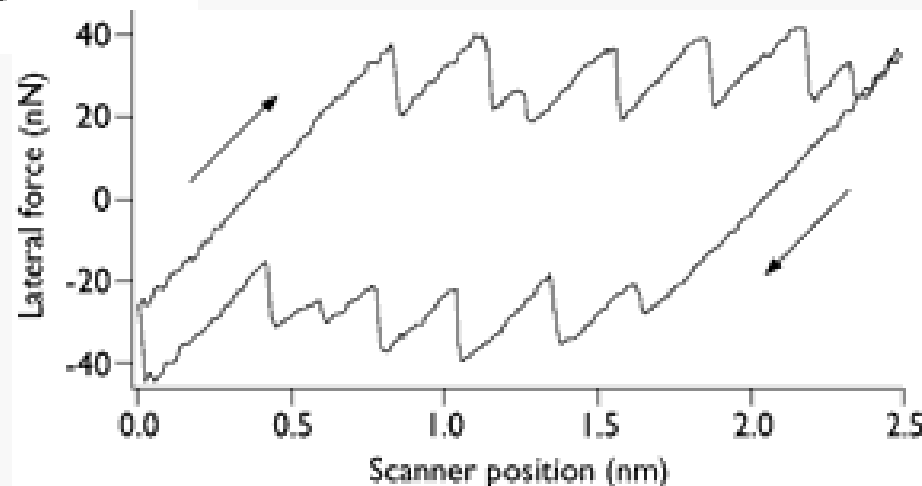
Frictional force microscopy



Poiché la tip si muove sul campione (a velocità di scansione) risente delle forze di attrito

La forza di attrito è letta come twisting della cantilever *di verso sempre opposto* allo spostamento (mentre le asperità topografiche hanno segno dipendente dalla topografia)

Nella scansione forward/backward si ottiene un loop che rappresenta l'energia dissipata



Microscopia a forza laterale (LFM, SFFM) II

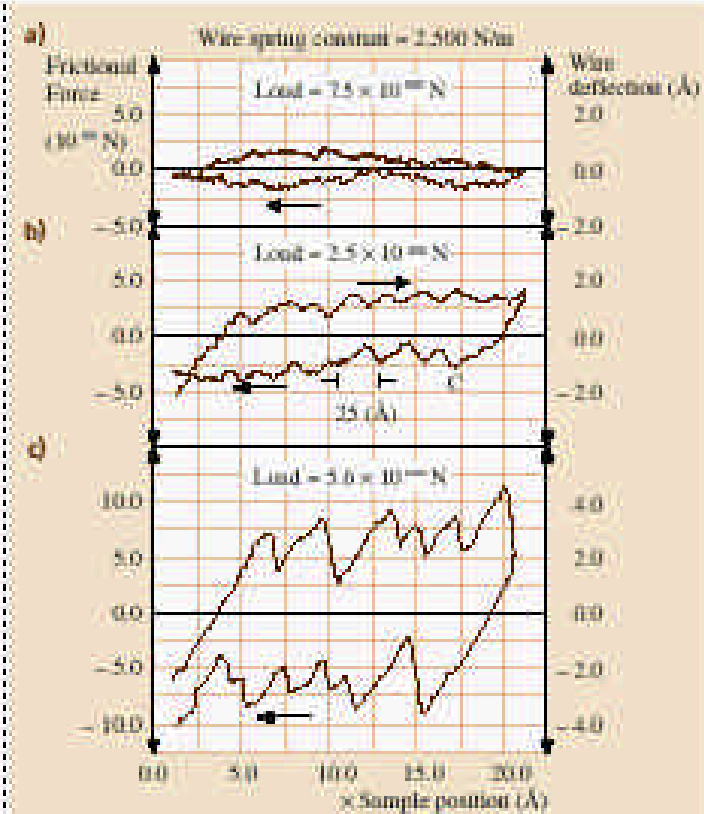


Fig. 20.19a-c Friction loops on graphite acquired with (a) $F_N = 7.5 \mu\text{N}$, (b) $24 \mu\text{N}$ and (c) $75 \mu\text{N}$. (After [20.1])

- ✓ Meccanismo di contrasto a livello atomico
- ✓ Possibilità di distinguere tra diversi materiali
- ✓ Informazioni nanotribologiche

Da B. Bhushan, Handbook of nanotechnology (Springer, 2003)

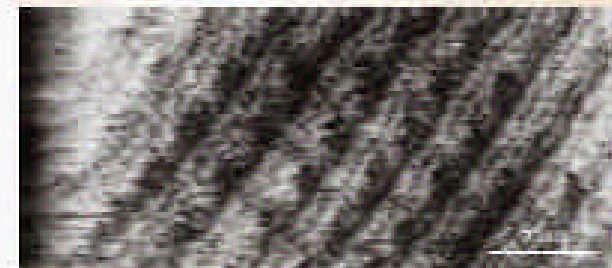


Fig. 20.18 (a) Topography and (b) friction image of Si(111)7x7 measured with a **PTFE** coated Si-tip. (After [20.29])

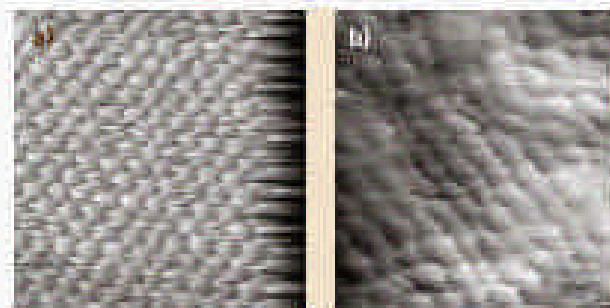


Fig. 20.19a,b Friction images of (a) Cu(111) and (b) Cu(100). Frame size: 3 nm. (After [20.34])

Microscopia a forza magnetica (MFM)

3.3.2 Magnetic Scanning Force Microscopy (MFM)

If a magnetic tip is used in the scanning force microscope, magnetic structures can be imaged. Magnetic scanning force microscopy is of interest, in particular, for the investigation of magnetic storage media. In the most general case, the magnetic force between sample and tip is

$$F_{\text{mag}} = -\nabla \int_{\text{tip}} \mathbf{M}_{\text{tip}} \cdot \mathbf{H}_{\text{sample}} dV \quad (13)$$

or

$$F_{\text{mag}} = (\mathbf{m}_{\text{tip}} \nabla) \mathbf{B}_{\text{sample}} \quad (14)$$

where $\mathbf{H}_{\text{sample}}$ and $\mathbf{B}_{\text{sample}}$ are the magnetic stray field and the magnetic induction of the sample, respectively. \mathbf{M}_{tip} and \mathbf{m}_{tip} are the magnetisation and the magnetic moment of the tip, respectively. Since in most cases the exact magnetic structure of the tip is not known, a model tip magnetization must be assumed. In the simplest case, the tip is a spherically structured magnetic single domain with the magnetisation \mathbf{M}_{tip} . Of particular interest are the stray fields of magnetic storage media which consist of different domains. Since the important aspect in force microscopy is not the forces but the force gradient, a pronounced variation of the signal is found near the domain walls, but not inside a domain. This situation is sketched in Figure 21. The parameter of the two curves shown (solid and broken lines) is the ratio of the working distance d and the radius R of the magnetic domain of the tip.

Figure 22a shows an experimentally measured picture of four different oriented magnetic domains. Images b and c show the fine structure of a 180° domain. Alternating bright and dark contrasts can be seen. These contrast changes show that the domain wall consists of segments with different wall orientation. This example illustrates that magnetic SFM is well suited for imaging magnetic structures that are commonly used in today's storage media.

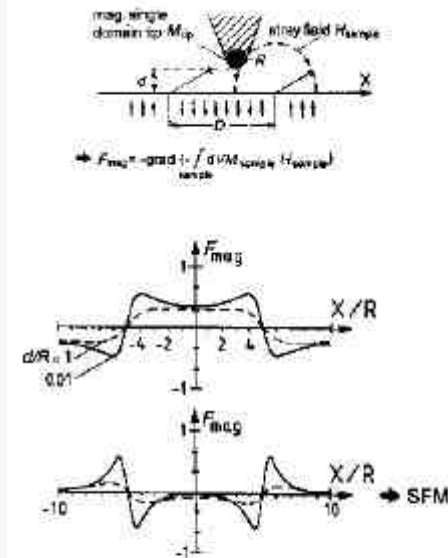


Figure 21: Principle of magnetic scanning force microscopy. On the left, the tip-sample configuration is shown and on the right the force and nominal force constant as a function of distance for this configuration. Two domain walls exist at position $X/R \approx +5$ and -5 (after [23]).

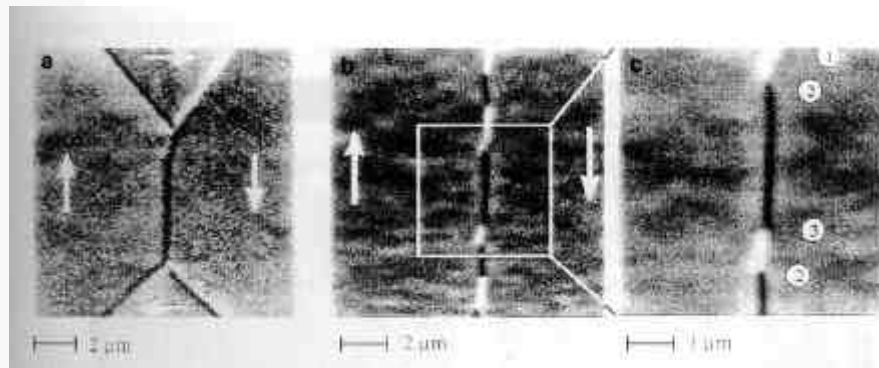


Figure 22: Magnetic SFM image of magnetic domains. (a) shows four domains of a Landau-Lifshitz structure in which the domain walls are the dark and bright lines. (b) and (c) show the fine structure of a 180° domain wall. The domain wall consists of segments with different wall orientation. Arrows denote the domain orientation. (after [26]).

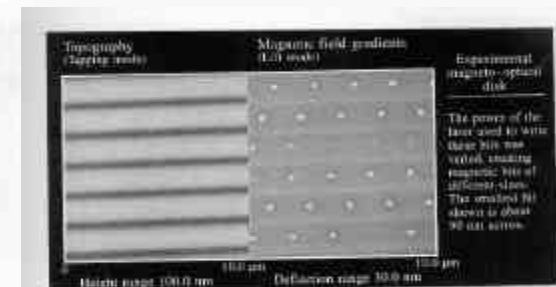


Fig. 5.21. A pair of images of a magneto-optical disk [5.26]

Microscopia a forza elettrostatica (EFM)

3.3.3 Electrostatic Scanning Force Microscopy (EFM)

The scanning force microscope can also be used for electrostatic or Coulomb images. In this case, however, the tip must be insulated. A modern version of electric force microscopes uses for the determination of surface charge or surface potential a complicated lock-in and phase loops electronics. The essential modification with respect to the old apparatus is the so called two-pass technique (LiftMode). In this method each line must be scanned twice. On the basis of two line scans, in which the first represents the topography of the surface in a contact mode and the second is taken at a fixed distance relative to the surface (Figure 23), one can reconstruct precisely the distribution of the charge or the potential on the surface without topographical error. In Figure 24 an example case is given, which highlights the possibilities of this modern tool for microelectronics. An other example showing an image of a broken carbon nano tube is represented in Figure 25.

Figure 23 shows the effect of the charge when the tip comes into the region of the local surface charge. An attractive Coulomb interaction exists between these charges and the charge induced in the tip. The electrostatic force as a function of distance is given by

$$F_{el} = -\pi\epsilon_0 U^2 \frac{r^2}{d^2} \quad (15)$$

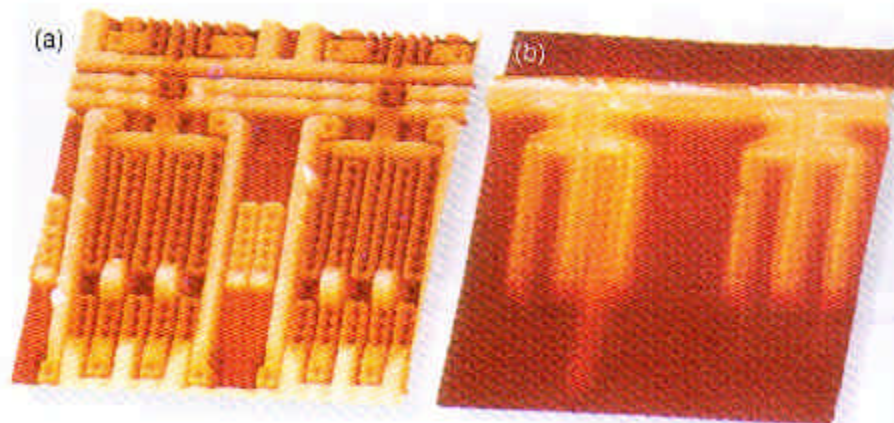
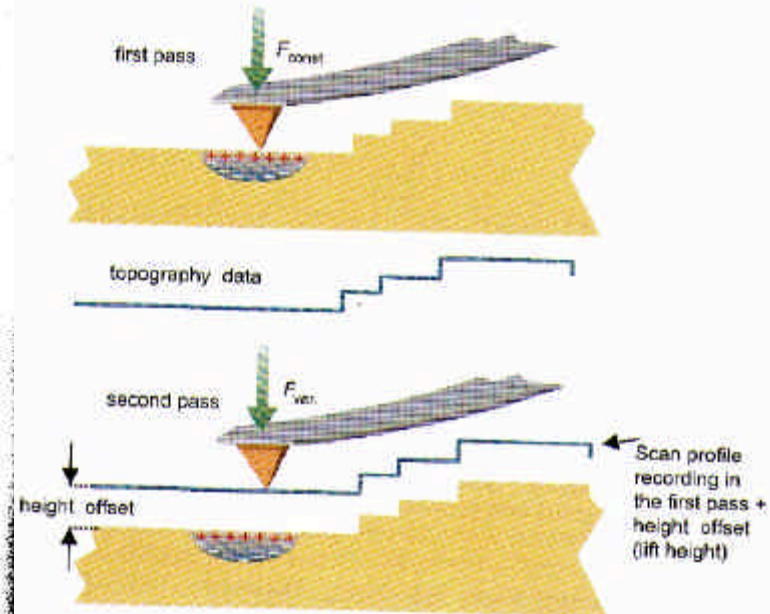


Figure 25: Schematic view of the two-pass SFM technique.

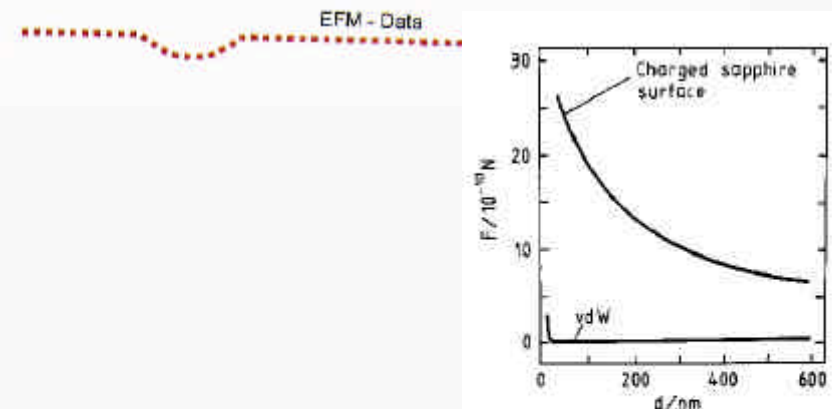
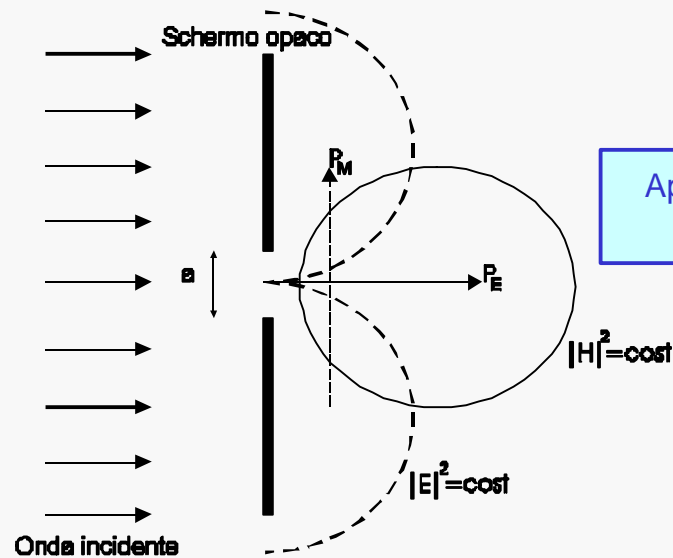


Figure 26: Comparison of the distance dependence of the electrical and van der Waals forces between a tip and a local electrical surface charge of $\pm 10^{-15} \text{ C}$ (after [23]).

Campo ottico prossimo I

Radiazione e.m. inviata su
apertura di dimensione
sotto lunghezza d'onda



Campo prossimo: radiazione e.m. non
propagante che si estingue su scala
dell'ordine dell'apertura

Aperture is a low-pass filter
for spatial frequencies

$$\Delta x \Delta k_x > 2\pi$$

$$E \propto \exp \left(iz \frac{2p}{l} \sqrt{1 - (lk_x)^2 - (lk_y)^2} \right)$$

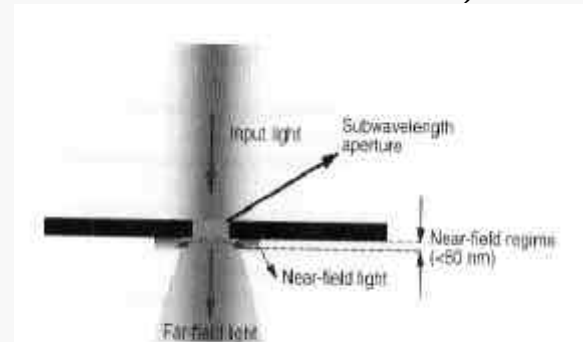
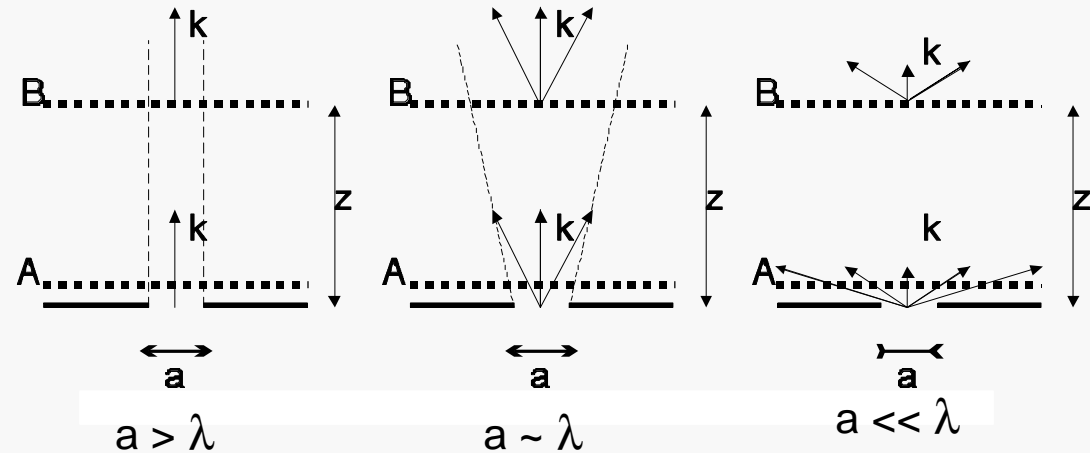


Figure 3.1. Principle of aperture controlled near-field optics.

Campo ottico prossimo II

3.2 THEORETICAL MODELING OF NEAR-FIELD NANOSCOPIC INTERACTIONS

Although Maxwell's equations provide a general description of electromagnetic phenomena, their analytical solutions are limited to relatively simple cases and rigorous treatment of nanoscale optical interactions presents numerous challenges. The various ways of approaching the theory of near-field optics can be classified according to the following considerations (Courjon, 2003):

- The physical model of the light beam
- The space chosen to carry out the modeling (i.e., the direct space or Fourier space modeling)
- Global or nonglobal way of treating the problem (e.g., performing separate calculation for the field in the sample and then computing the capacity of the tip to collect the field)

Among several methods used for electromagnetic field calculation, one can distinguish techniques derived from the rigorous theory of gratings like the differential method (Courjon, 2003) and the Reciprocal-Space Perturbative Method (RSPM), as well as techniques that operate in direct space like the Finite-Difference Time-Domain Method (FDTD) and the Direct-Space Integral Equation Method (DSIEM).

In general, analytical solutions can provide a good theoretical understanding of simple problems, while a purely numerical approach (like that of the FDTD method) can be applied to complex structures. A compromise between a purely analytical and a purely numerical approach is the multiple multipole (MMP) model (Girard and Dereux, 1996). With the MMP model, the system being simulated is divided into homogeneous domains having well-defined dielectric properties. Within individual domains, enumerated by the index i , the electromagnetic field $f^{(i)}(\mathbf{r}, \omega_0)$ is expanded as a linear combination of basis functions

$$f^{(i)}(\mathbf{r}, \omega_0) \approx \sum_j A_j^{(i)} f_j(\mathbf{r}, \omega_0) \quad (3.1)$$

where the basis functions $f_j(\mathbf{r}, \omega_0)$ are the analytical solutions for the field within a homogeneous domain. These basic functions satisfy the eigenwave equation for the eigenvalue q_j (analogous to the equation in Table 2.1):

$$-\nabla \times \nabla \times f_j(\mathbf{r}, \omega_0) + q_j^2 f_j(\mathbf{r}, \omega_0) = 0 \quad (3.2)$$

MMP can use many different sets of basis fields, but fields of multipole character are considered the most useful. The parameters $A_j^{(i)}$ are obtained by numerical matching of the boundary conditions on the interfaces between the domains.

As an example of the use of this technique for investigations of nonlinear optical processes in the near field, we show here investigations of second harmonic generation in a noncentrosymmetric nanocrystal exposed to fundamental light from a near-field scanning tip (Jiang et al., 2000).

One notes that a consequence of nonlinear optical interaction in the near-field is that the phase-matching conditions do not need to be fulfilled because the domains are much smaller than the coherence length. Starting from Maxwell's equations, the electric fields of the fundamental and the second harmonic (SH) wave can be shown to satisfy the nonlinear coupled vector wave equations

$$\nabla \times \nabla \times \mathbf{E}(\mathbf{r}, \omega_0) - \frac{\omega_0^2}{c^2} \epsilon(\mathbf{r}, \omega_0) \mathbf{E}(\mathbf{r}, \omega_0) = 4\pi \frac{\omega_0^2}{c^2} \mathbf{P}^2(\mathbf{r}, \omega_0) \quad (3.3)$$

$$\nabla \times \nabla \times \mathbf{E}(\mathbf{r}, 2\omega_0) - \frac{4\omega_0^2}{c^2} \epsilon(\mathbf{r}, 2\omega_0) \mathbf{E}(\mathbf{r}, 2\omega_0) = 4\pi \frac{4\omega_0^2}{c^2} \mathbf{P}^2(\mathbf{r}, 2\omega_0) \quad (3.4)$$

where $\epsilon(\mathbf{r}, \omega_0)$ and $\epsilon(\mathbf{r}, 2\omega_0)$ are linear dielectric functions for the fundamental and the SH waves, respectively.

The propagation constant k_z along the z direction is

$$k_z = (k^2 - k_0^2)^{1/2} = k_0(1 - n_1^2 \sin^2 \theta)^{1/2} \quad (3.5)$$

where $k_0 = 2\pi/\lambda$, λ is the wavelength of illumination light in free space; n_1 is the refractive index of the tip, and θ is the incident angle. If $1 - n_1^2 \sin^2 \theta > 0$ (i.e., k_z is real), the waves will propagate with constant amplitude between the probe and the sample, which corresponds to the "allowed light" in the sample. In the areas where k_z is imaginary, the waves will decay exponentially within distances comparable to the wavelength, thus such waves have evanescent character and produce the "forbidden light" in the sample. From the electrical field distribution of the fundamental wave calculated with the MMP method, we can obtain the electrical field distribution of the SH wave and the different contributions of "allowed light" and "forbidden light."

Necessità di complicati metodi numerici per descrivere il campo prossimo

Da P.Prasad, Nanophotonics (Wiley, 2004)

Campo ottico prossimo III

Figure 3.4 shows the three-dimensional perspective view of the optical near-field intensity of the fundamental and the SH wave, respectively. The field intensity of SH wave is orders of magnitude weaker than that of the fundamental wave (FW), and it is highly localized within the area of the probe tip center—that is, about $50 \text{ nm} \times 50 \text{ nm}$. The fundamental wave is more delocalized compared to the SH wave.

Figure 3.5 shows the sectional plot of Figure 3.4 along the x -axis direction, and Figure 3.6 shows the integration of $|E|^2$ for the SHG over the total solid angle. It is

clear that the field intensity close to the probe center comes almost entirely from the allowed light, while a field enhancement appearing at the edge of the tip is due to the field components from the forbidden light. The field intensity decreases very rapidly with the tip-sample distance, and its typical decay length is approximately equal to the tip size—that is, about 50 nm . Furthermore, the field intensity of the forbidden light, which decays exponentially, exhibits a much larger variation with the probe-sample distance than does the field intensity of the allowed light. Figure 3.6 also indicates that when the probe is very close to the sample surface—that is, $d < 50 \text{ nm}$ —the intensity from the forbidden light dominates. However, when the probe-sample distance is larger than 50 nm , the intensity from the allowed light becomes the main contribution to the total field intensity. Because the allowed light only contains the low spatial frequencies of the sample surface, the detection of the forbidden light is essential to investigate details for both linear and nonlinear optical interactions.

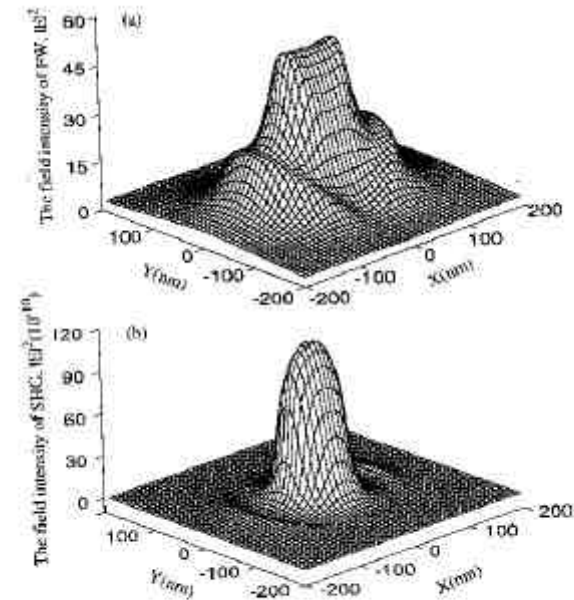
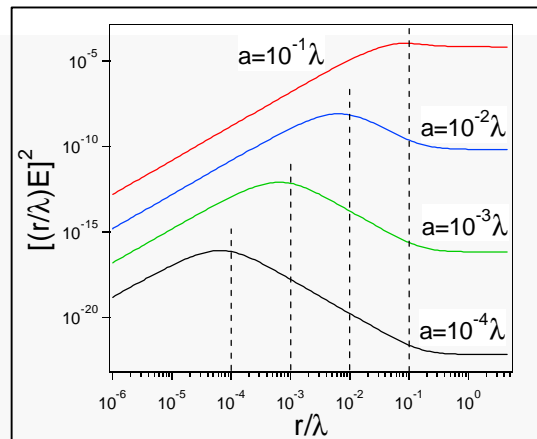


Figure 3.4. Three-dimensional perspective view of the optical near-field intensity of (a) the fundamental wave and (b) the second harmonic generation. The calculation is performed for λ -normalization and for the tip-sample distance of 10 nm .

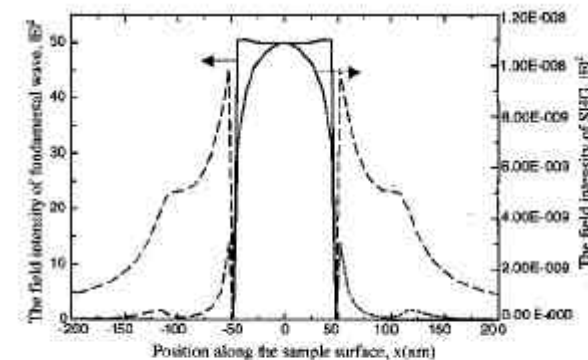


Figure 3.5. The electric field intensity of the fundamental wave and the second harmonic generation along the sample surface for tip-sample distance of 10 nm . The solid curve denotes the field intensity of the allowed light; the dashed curve denotes the field intensity of the forbidden light.

Rivelazione in campo lontano

7.2.1 Ray Optics of a SNOM

SNOM techniques differ mainly in the types of probes which are used and also by their ray optical components, i.e., their optical scheme, which is useful for a classification of most types of SNOM concepts. As shown schematically in Fig. 7.4, three different regions where the rays propagate can be distinguished: I) the body of the probe, II) the outside and III) the substrate of the object. In general, regions I and III will have a higher refractive index than the outside region II. Different angular domains of rays propagating in regions I and III exist, which can be distinguished by the criterion of total reflection of a ray falling on its boundary or of it being partially refracted into the outside II. Thus, in the case of a transparent substrate III, we distinguish between the angular domain III₁ of angles ε with $-\varepsilon_t < \varepsilon < \varepsilon_t$, where ε_t is the critical angle of total reflection ($\varepsilon_t = 41.5^\circ$ for glass of refractive index 1.5) and the angular domain III₂ with $90^\circ > \varepsilon > \varepsilon_t$ or $-90^\circ < \varepsilon < -\varepsilon_t$, which is sometimes called the range of forbidden light. Rays of the domain III₂ are totally reflected in the substrate, whereas rays of domain III₁ are partially refracted into the outside II. Also within the body of the tip I two different domains may be distinguished (Fig. 7.4). This figure only shows the case of a rectangular wedge, a two-dimensional analog of the three-dimensional body of the tip. For such a wedge, with a refractive index $n = 1.5$, rays entering at an angle within the angular domain ($-3.5^\circ < \varepsilon < +3.5^\circ$, region I₂) will be totally reflected back into a reflected ray of the same angle ε . Rays entering the wedge at different angles will also be reflected into the same angle and be partially refracted into the outside II of the wedge. This situation also applies, if the wedge is coated with a partially transparent metal film, as is typical for SNOM probes. Similar considerations also apply for a three-dimensional tip.

In summary, in many cases it is possible to distinguish in regions I and III between angular domains I₁ and III₁ where total reflection of the rays occurs into the same domain and the domains I₂ and III₂ from where light is partially refracted to the outside II.

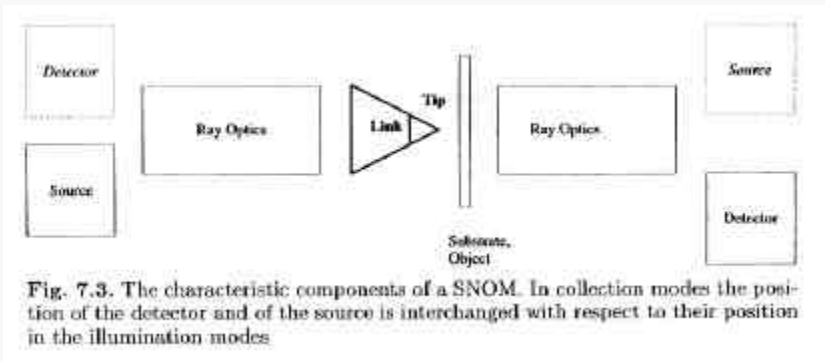


Fig. 7.3. The characteristic components of a SNOM. In collection modes the position of the detector and of the source is interchanged with respect to their position in the illumination modes

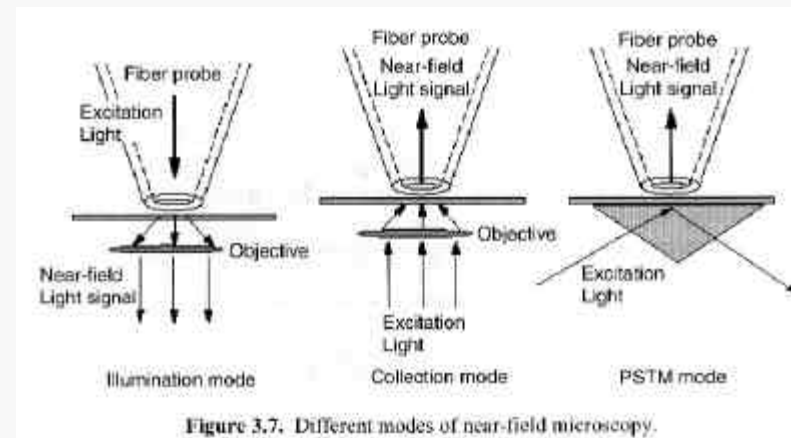
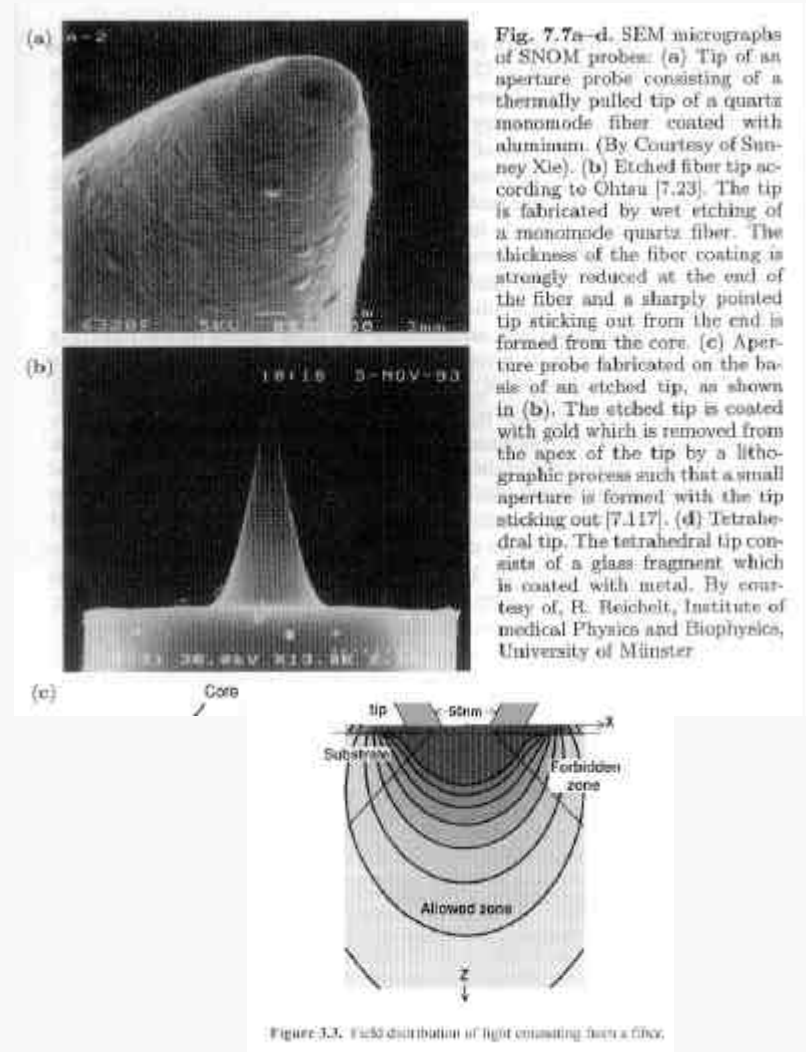
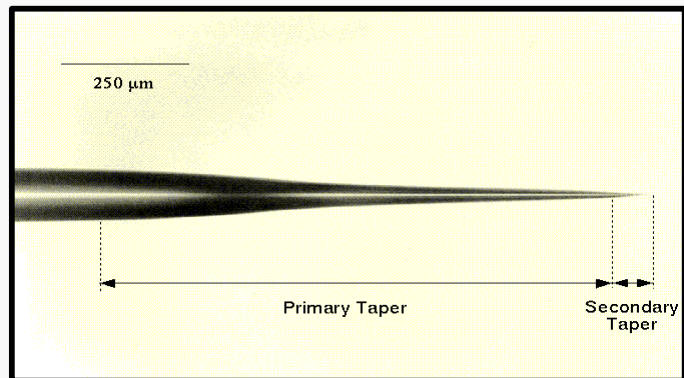


Figure 3.7. Different modes of near-field microscopy.

L'eccitazione con campo prossimo produce (es., per scattering, o fotoluminescenza) radiazione convenzionale analizzabile in campo lontano

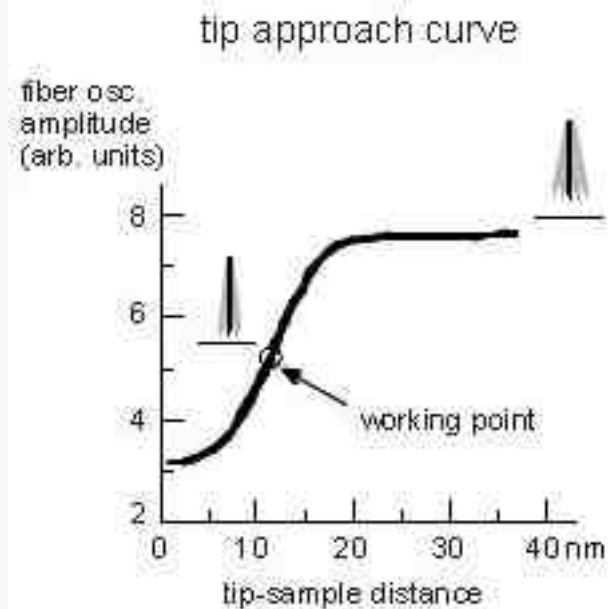
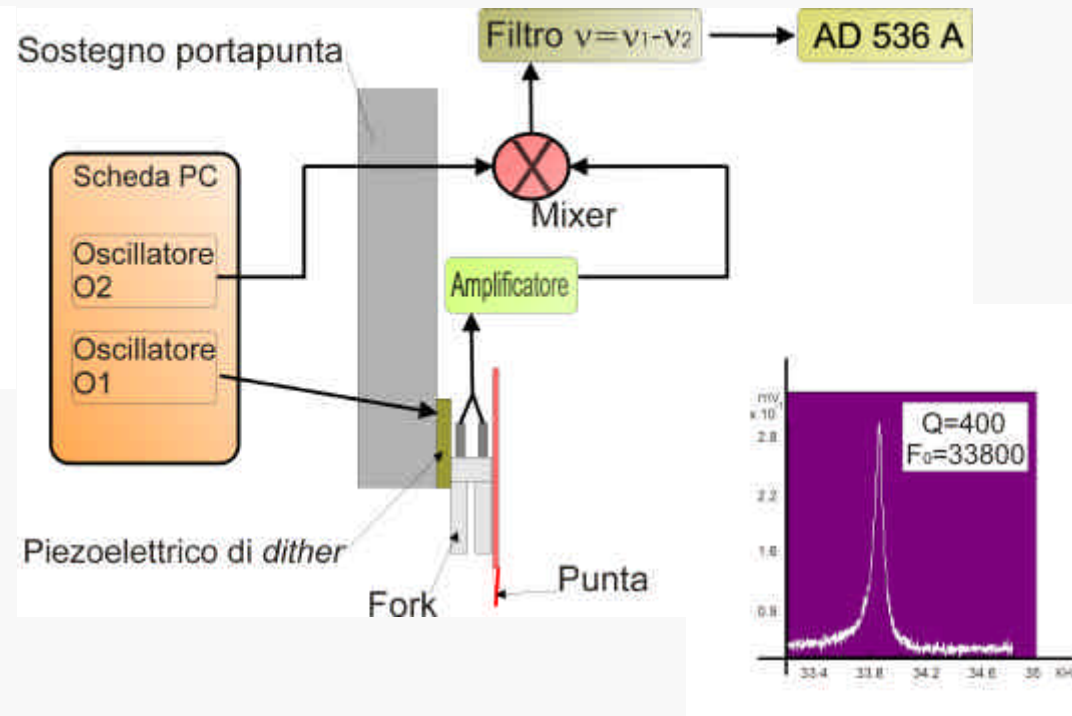
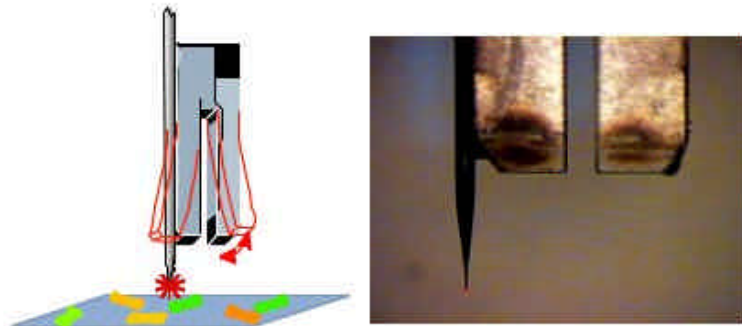
Probes per microscopi a scansione di campo ottico prossimo (SNOM ad apertura)

Probe: tapered optical fiber, with metalization and apical aperture
 $a \ll \lambda$ (aperture-SNOM)



Dimensioni tipiche dell'apertura: 50-100 nm

Controllo distanza tip-campione



Punta mantenuta in oscillazione rapida parallelamente alla superficie del campione (movimento di dithering)
 A distanza < 10 nm **shear-force** riduce l'oscillazione
 L'ampiezza di oscillazione è letta con tuning-fork e usata nel controllo di feedback

In ogni scansione si acquisisce anche la topografia

Alcuni modi di operazione dello SNOM

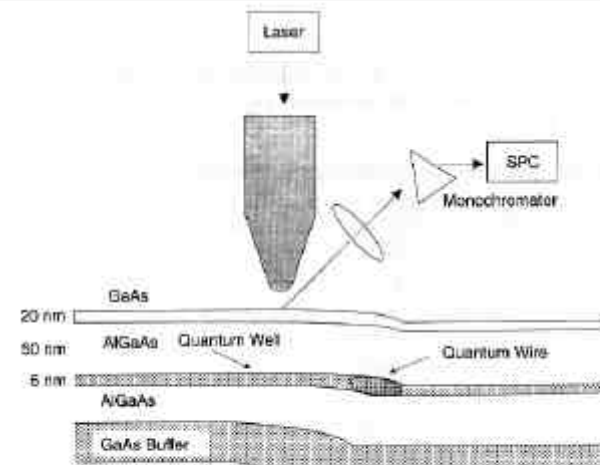
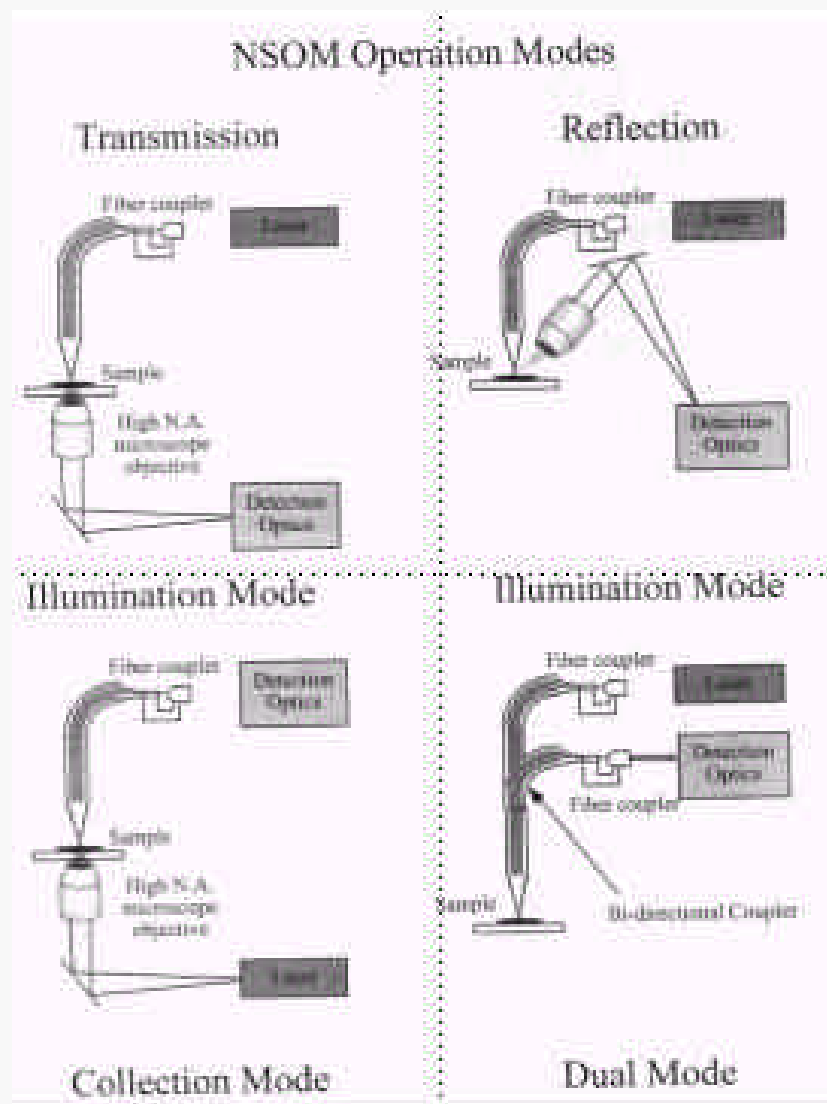


Fig. 7.22. Scheme of SNOM setup to record PL and PLE spectroscopic SNOM images and schematic view of quantum wire, which is embedded into a quantum well

Il campo prossimo può essere *prodotto* (illumination mode) o *raccolto* (collection mode) dalla probe

SNOM senza apertura

3.5 APERTURELESS NEAR-FIELD SPECTROSCOPY AND MICROSCOPY

As mentioned in Section 3.3, an emerging approach is the apertureless near-field spectroscopy and microscopy (Novotny et al., 1998; Sanchez et al., 1999; Bouhelier et al., 2003). The use of an aperture such as a tapered fiber opening poses a number of experimental limitations. Some of these are:

- Low light throughput due to the small fiber aperture and the finite skin depth (light penetration) into the aluminum metal coating around the tapered fiber.
- Absorption of light in the metal coating: this can produce significant heating that can create a problem in imaging, particularly of biological samples.
- Pulse broadening in the fiber, when using short pulses for nonlinear optical studies. Also, the fiber tip may be damaged by the high peak intensity as already discussed in Section 3.3.

The apertureless approach overcomes these limitations, at the same time providing a significantly improved resolution. It has been demonstrated by Novotny, Xie, and co-workers (Sanchez et al., 1999; Hartschuh et al., 2003; Bouhelier et al., 2003) that optical images and spectra of nanodomains ≤ 25 nm can be obtained using the apertureless near-field approach involving a metal tip of end diameter ≤ 10 nm.

The two approaches used for apertureless NSOM are:

1. Scattering type, which involves nanoscopic localization and field enhancement of the electromagnetic radiation by scattering of the light from a metallic nanostructure. An example is provided by Figure 3.2 where the light is scattered by a sharp metallic tip. Scattering and field localization can also be produced by a metallic nanoparticle within nanometers of distance from the sample surface. The localization and enhancement of electromagnetic field by plasmon coupling to a metallic nanoparticle is discussed in Chapter 5 under "Plasmonics." This principle of obtaining nanoscopic resolution using scattering from a metallic nanoparticle also forms the basis of "plasmonic printing," discussed in Chapter 11 on "Nanolithography".
2. Field-enhancing apertureless NSOM, where a metallic tip is used to enhance the field of an incident light in the near field. In this case, the light is incident on the tip as a normal propagating mode (far-field). The strongly enhanced electric field at the metal tip produces nanoscopic localization of optical excitation. This approach offers simplicity and versatility of using light by just focusing on the metallic tip through a high-numerical-aperture lens. Hence it is described here in detail, with examples of some recent studies utilizing this approach.

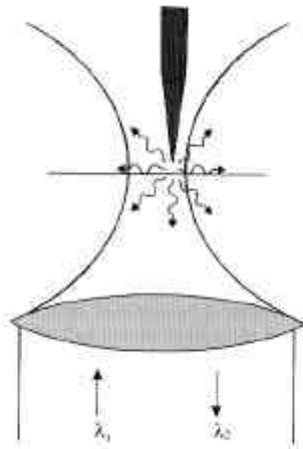


Figure 3.22. Metallic tip enhancing the local field by interacting with the focused beam at λ_1 . The optical response at another wavelength λ_2 is collected by the same objective lens.

Una nanoparticella (o una nanopunta) scattera il campo propagante producendo un campo prossimo

Vantaggi:

- Risoluzione (fino a sotto 10 nm??)
- Intensità del campo prossimo (le probes a fibra ottica hanno typ. throughput $< 1/10000$)

Esempi SNOM (fotoluminescenza)

Saiki et al. (1998) and Matsuda et al. (2001) conducted room temperature photoluminescence study on a single quantum dot from InGaAs quantum dots grown on a GaAs substrate. Their result is shown in Figure 3.12. Because of the spectral resolution obtained by sampling only a single quantum dot (no inhomogeneous broadening), they were able to observe, at an appropriate excitation density, emission not only from the lowest level (subband) of the conduction band but also from higher levels. (See Chapter 4 for a description of these bands.) They were able to study the homogeneous line width, determined by the dephasing time of excitation (see Chapter 6 for a description of dephasing time), as a function of the interlevel spacing energy. They found that the line width was larger for a smaller-size quantum dot for which the interlevel spacing is larger. (This is predicted by a simple particle in a box model as the length of the box becomes smaller, see Chapters 2 and 4.)

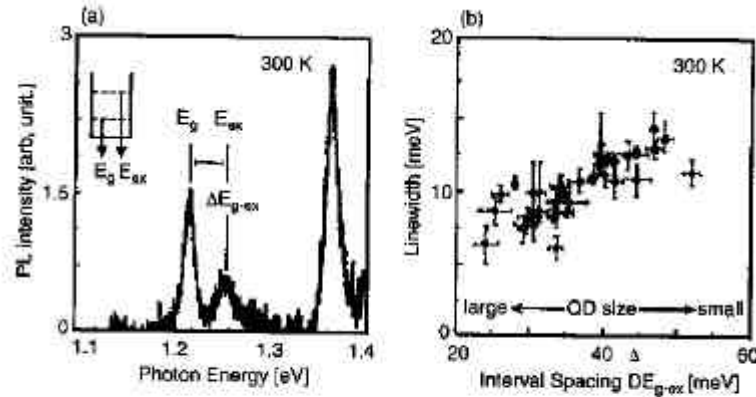


Figure 3.12. Photoluminescence spectrum of single QD at room temperature (a), and dependence of the homogeneous linewidth of ground-state emission on interval spacing, which is closely related to size of Qd's (b). From Saiki and Narita (2002), reproduced with permission.

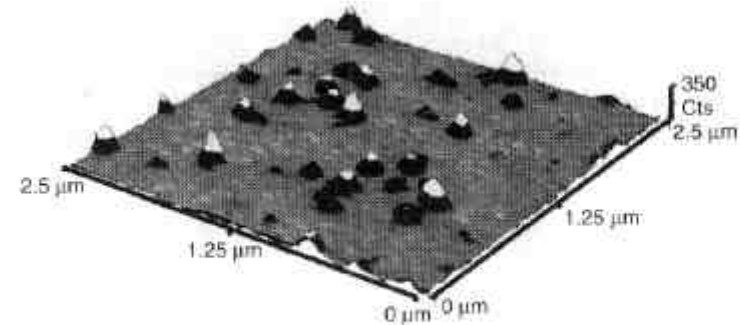


Figure 3.13. Fluorescence NSOM images of single molecules. From Professor D. Higgins and Professor P. Barbara, unpublished results.

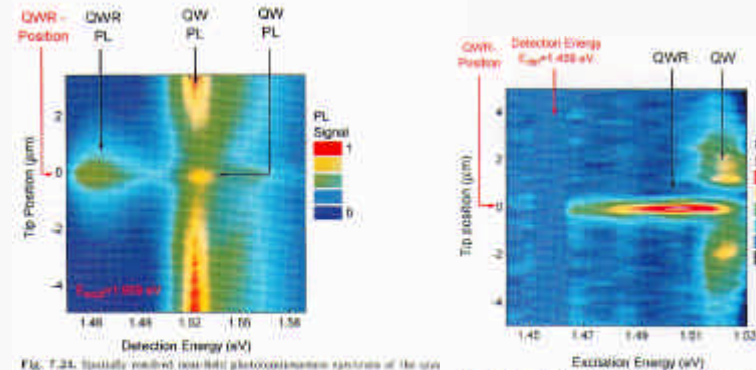


Fig. 7.24. Spatially resolved near-field photoluminescence excitation spectrum of the quantum wire heterostructure. The spectrum was recorded by spatially resolved excitation of the sample at 1.55 eV. The tip was scanned along the lateral direction perpendicular to the wire. The PL intensity (in arbitrary units) is plotted as a function of the position and detection energy. The color bar corresponds to high, white, gray, and blue to low PL intensity. The quantum wire structure is shown schematically in the inset. Note that, in addition to the first quantum well intersubband at 1.55 eV, a further, slightly blue-shifted, second quantum well intersubband is resolved.

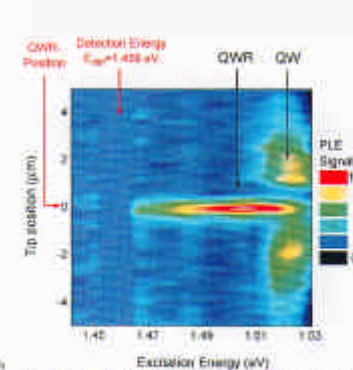


Fig. 7.25. Spatially resolved near-field photoluminescence excitation spectrum. The PL signal is plotted as a function of tip position and excitation energy. The scan direction is perpendicular to the wire. The photoluminescence was detected at 1.50 eV. The color bar corresponds to high and purple to low intensity.

Da Wiesendanger Ed., Scanning Probe Microscopies (Springer, 1998)

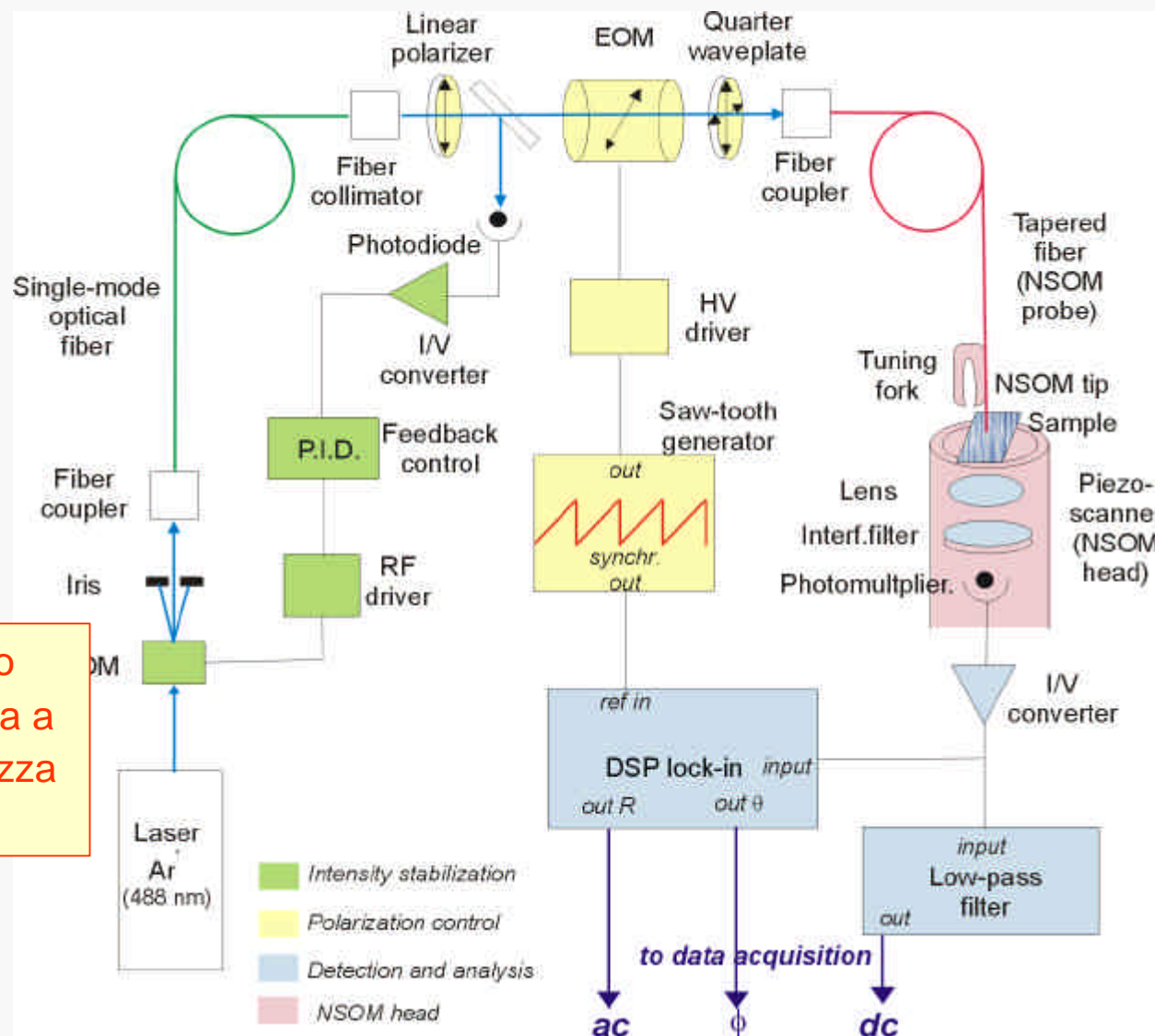
Spettroscopia ottica su singole nanostrutture o singole molecole

SNOM a modulazione di polarizzazione (PM-SNOM)

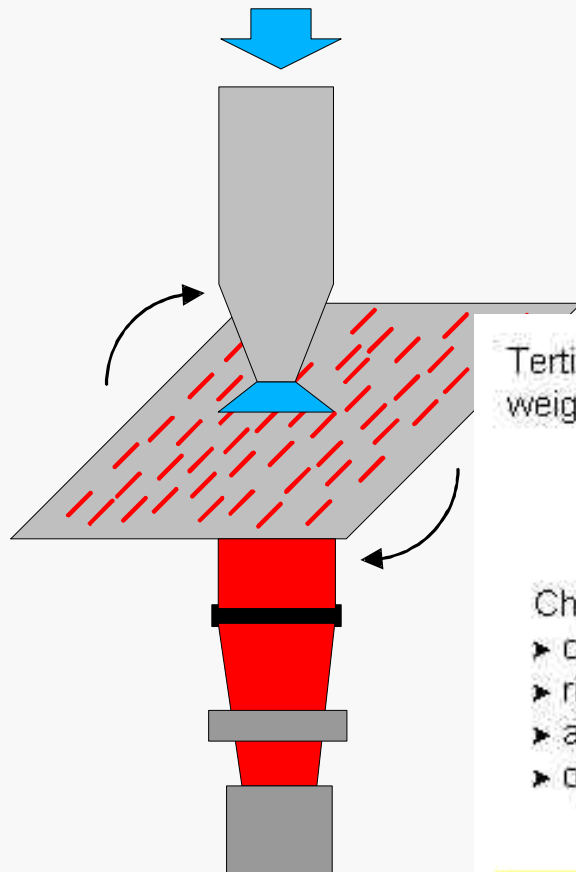
La polarizzazione della luce che entra nella probe è lineare rotante

Polarimetria (cioè studio dell'attività ottica) trasferita a scala locale, sotto lunghezza d'onda

Michele Alderighi, Tesi di Laurea in Scienza dei Materiali, Pisa 2003

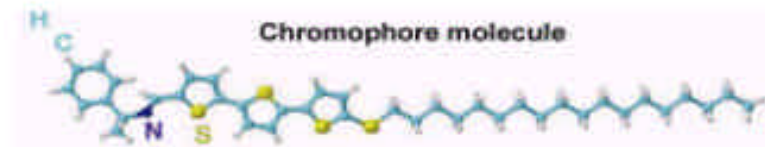


PM-SNOM II



PM-SNOM impiegato per analisi di campioni host-guest (cromoforo in matrice polietilenica stirata) con elevato dicroismo lineare

Tertioophene-like chromophore dispersed (3% wt) in a ultra-high molecular weight polyethylene (UHMWP)



Chromophore choice:

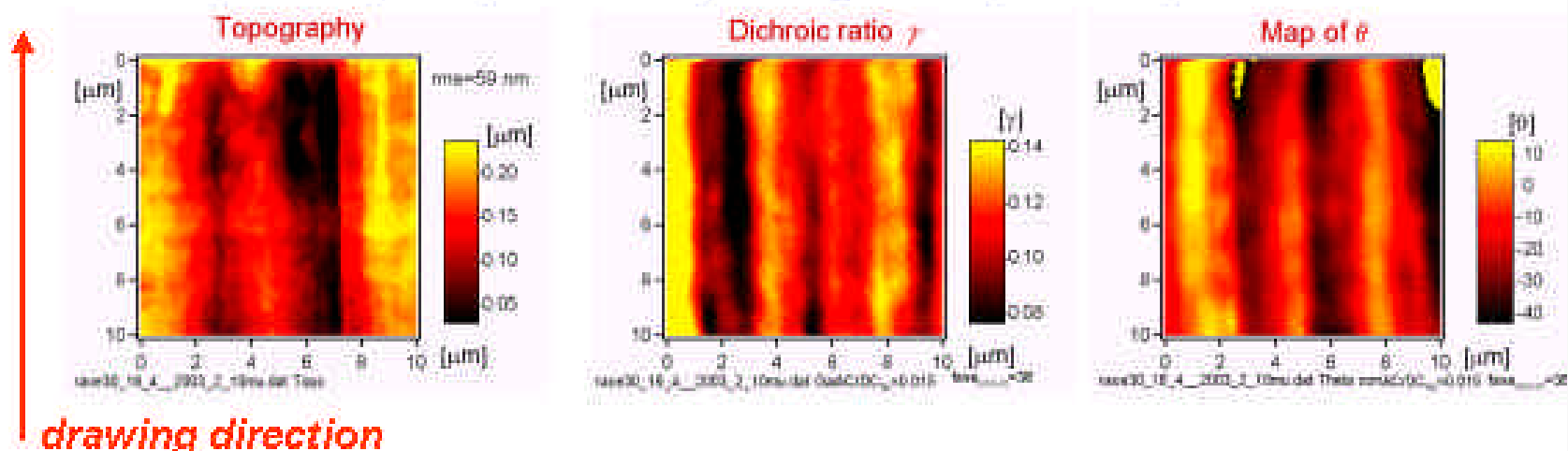
- chemical compatibility with the host;
- rigid structure;
- absorption in the blue (peaked around 400 nm);
- optical activity (right- and left-handed isomers available).

Fabrication process (at Dipartimento di Chimica e Chimica Industriale, Università di Pisa, group of Prof. Ciardelli and Prof. Ruggeri):

- cast (to obtain pristine films) followed by
- high temperature drawing (to obtain films with stretched polymer chains)

PM-SNOM III

Sample: L-R (50:50) stretched (drawing ratio 30), 10x10 μm scan



Topographical variations
due to local changes in
polymer chain stretching

Local optical activity strongly affected by (host) stretching

Chromophore molecules follow host molecule alignment
Macroscopic dichroism ($\gamma \sim 0.1$ in this sample) due to the combined effect of elongated islands with locally inhomogeneous optical activity

Introduzione: nanomanipolazione con SPM

Obiettivi generali:

Sfruttare le possibilità di controllo subnanometrico della posizione della sonda per (e.g.):

- Manipolare (la posizione) di nanoparticelle o **unità elementari** su superfici;
- Produrre **modificazioni locali** di substrati (indentazioni, reazioni chimiche, litografie, etc.)

5 Manipulation of Atoms and Molecules

The scanning probe microscopes do not only have the ability to image individual atoms. The interaction needed for imaging the surfaces can also be used to manipulate individual adatoms, molecules, or the surface structure itself on the atomic scale. Indeed a large number of works concentrated on the manipulation of individual atoms and in the following novel nanostructures were built. Here we briefly show the work by Eigler and coworkers [44], [45] as examples, followed by a more subtle tip-induced manipulation of atoms, and the tip-induced migration of defects by tip-induced excitement of defects [46], [47]. More recently the group of Rieder could even perform full chemical reactions with single molecules [48]. Three different manipulation modes can be distinguished: the lateral and the vertical manipulation as well as the tunnel current induced changes. The combination of all three modes enables to achieve tip controlled chemical reactions.

Nanomanipolazione ed
imaging con le stesse
tecniche

Da R. Waser Ed., Nanoelectronics and
information technology (Wiley-VCH,
2003)

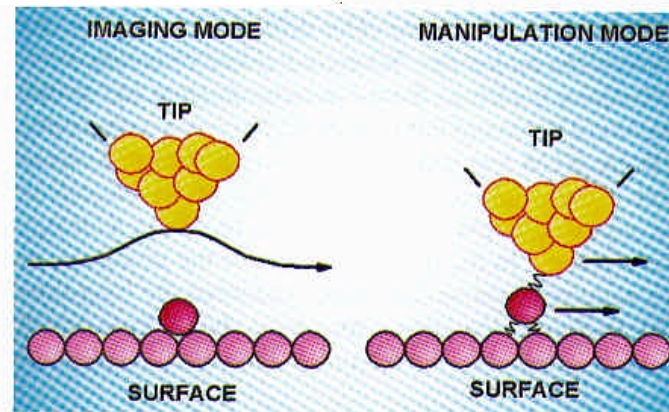


Figure 32: In the STM imaging mode the tunnel current is kept constant and the cantilever is raised. For manipulation the tip is lowered above an atom dragging it to the desired position, lifting the cantilever losing interaction with the atom [44].

Impiego dell'STM in nanomanipolazione

In the STM device, the tip is so close to the target as to make the electron current highly spatially confined - it is the key to the extremely high spatial resolution of STM images. The key element in surface modifications is also the STM tip. To affect these modifications one utilizes a variety of tip-sample interactions, including attractive and repulsive forces, electric fields, and the effect of highly spatially confined electron currents. The small distance between tip and sample, which is about one nanometer, causes electrons to tunnel to (or from) a region on the sample that is approximately one nanometer in diameter, with an even smaller major distribution area. Thus, the surface fabrication produced by STM must be performed on the nanometer scale, i.e., STM can nanofabricate. Later, we will see that it is also possible to manipulate a single atom or molecule adsorbed on the surface with STM.

Since the invention of STM in 1981, as a nanofabrication tool it has been used in direct surface identification, electron-beam-induced deposition, etching, single-atom manipulation, and so on. All of these techniques have a wide-spread application potential. First, it is possible to reduce the linewidth of large-scale integrated circuits from the micrometer scale to the nanometer scale by lithography, beam-induced deposition and etching, which is one of the goals of high technology. In most cases the resulting feature with dimensions on the order of hundred nm [9.1], but features with dimensions of a few nm have also been achieved [9.2-4]. An exciting possibility will be to use the tip to "operate" on biomolecules such as DNA and proteins. The electronic properties of devices may be dominated by quan-

tum-size effects when their size is reduced to the nanometer or atomic scale. By STM and other techniques, it is possible to discover new phenomena, design new devices and fabricate them. Next, STM can be utilized to repair masks and integrated circuits. The surface topographies can be imaged in situ during the surface fabrication process by STM, which makes it possible to discover defects in masks and circuits, to repair them by surface deposition and etching, and then to examine the final results by STM. Lastly, using the STM as a tool, the essential research on the growth, migration and diffusion of clusters on surfaces, and the interactions between small particles or between substrates and particles can be performed in order to manipulate clusters or atoms on purpose.

Lens-focused electron beams, ion beams and X-rays can also be employed in nanofabrication. Although the STM seems unlikely to become competitive in some areas of nanofabrication such as wafer-scale resist patterning, it has its own characteristics. First, an STM can work in either the tunneling mode or the field-emission mode. When working in the latter, a low applied voltage (higher than a few volts) can produce a strong enough electric field to make electrons emit from the tip over the barrier, because the distance between tip and sample is very small. These emitting electrons with a certain current and energy, will not diverge greatly because of the small separation which results in a nanometer beam diameter on the substrate surface. Unlike conventional high-energy electron lithography, the low-energy STM beam reduces the problems associated with electron backscattering and the generation of secondary electrons. A resolution of about 10 nm, and exposure rates comparable to those of conventional electron lithography have been achieved. Secondly, by moving the tip to contact the sample, the STM tip can also produce local contact forces and electrostatic forces in a small region on the sample surface to create indentations directly. Lastly, at present, STM is the only instrument that can provide a nm-sized beam of very low energy electrons ($0 \div 20$ eV). The importance of electrons with low energy is obvious when it is considered that many of the processes such as migration, bond breaking, chemical reactions that would be interesting to control, have activation energies less than 10 eV per atom which require a low-energy beam.

Modificazioni e/o manipolazioni su scala nanometrica mediante STM sfruttano numerosi fenomeni

Manipolazione laterale di particelle su substrato

5.1 Lateral Manipulation

In the lateral manipulation mode a particle on the sample surface is moved along the surface to the desired location without losing contact to the surface. The motion can be obtained either by dragging or pushing. Figure 31a to d show the build up of a quantum corral by manipulating individual Fe atoms on a Cu(111) surface at 4 K [44]. The final structure of 15 nm diameter consists of 48 Fe atoms. At this stage one may ask how such a fine manipulation can be achieved. The procedure is as follows: Fe atoms are evaporated onto a Cu(111) surface cooled to 4 K. The surface containing statistically distributed Fe atoms is then examined by STM. Normally, no atoms are displaced, but if the distance between tunnelling tip and a Fe atom is reduced, then the tunnelling tip exerts an attractive force on the Fe atom and the Fe atom can be dragged by the tunnelling tip to the desired location on the surface [44], [45]. Once the desired location is reached, the tip is retracted. Increasing the distance between the tip and the sample reduces the tip-Fe atom interactions and, hence, the Fe atom remains at its new position (Figure 32). Figure 31e shows that in this way a whole circle of iron atoms can be built up. The artificially build nanostructure shown in Figure 31 confines the electrons of the two-dimensional surface electron gas on Cu(111). Therefore, as soon as the circle is complete, the electrons are scattered in the circle and form standing electron waves due to quantum mechanics. Figure 31e thus illustrates the wave nature of the electrons.

In a quantum well, due to the quantization of the electron states, not only standing electron waves but also discrete energy values of the electrons are expected. Consequently, increased electron densities should occur at specific energies. As already described, the density of states can be approximately calculated from experimentally measured current-voltage characteristics by calculating $(dI/dV)/(I/V)$. For metals, however, I/V is generally constant and the sample density of states is therefore proportional to dI/dV . The variation of dI/dV as a function of voltage reflects the density of states variation as a function of energy. Figure 33 shows the density of states thus obtained for three different surface positions. At the centre of the circle, as expected, peaked energy levels occur (curve a), whereas outside the circle no structure in the density of states is measurable (curve c). If the density of states is measured at a distance of 0.9 nm from the circle centre, even more energy levels occur as shown by the arrows in curve b.

This example of spectroscopic measurements and of the spatial distribution of the electron waves in a potential well provides a particularly illustrative picture of quantum mechanics. The construction of different quantum structures by an atom-by-atom manipulation approach using scanning probe microscopes nowadays allows a new look into the quantum world and a direct spatial measurement of the electron waves.

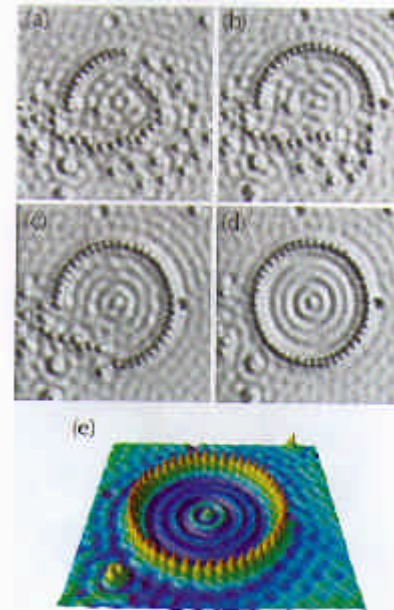


Figure 31:
(a) to (d) show the process of building a quantum corral consisting of 48 Fe atoms positioned on a Cu(111) surface. The resulting structure and the standing waves induced by the quantum confinement of surface electrons in the structure is visible in the three-dimensional view (e) of the quantum corral [44].

Fe quantum corral

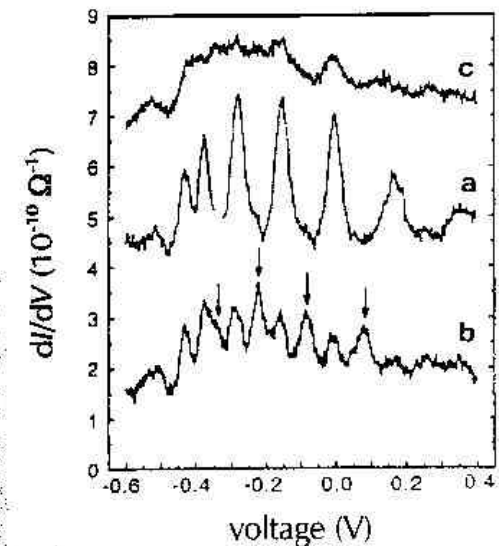


Figure 33: Scanning tunneling spectra obtained for different positions in the quantum corral of Figure 16. The spectra were obtained (a) in the circle centre, (b) 0.9 nm from the circle centre, and (c) outside the circle. A clear quantization of states can be seen inside of the circle. [44].

Fabbricazione di “strutture quantiche” artificiali
(con nuove potenzialità)

Manipolazione laterale e ricostruzione substrato

Instead of evaporating foreign atoms onto a copper surface it is also possible to reconstruct the substrate surface itself, which is more difficult due to the higher coordination number and binding energy of the atoms located in the surface or in steps [49]. The experiments shown here are carried out on Cu(211) substrates at 30 – 40K. In Figure 34 a sphere model of the copper surface is shown, whereby the atoms are shaded darker the deeper they lie. Lateral manipulation of single Cu atoms parallel and perpendicular to step edges is presented in Figure 35 [49]. A measure for the minimum force necessary to move a copper atom is the tunnel resistance which displays the distance between tip and sample. The tunnel resistance used for motion along a step edge was approx. 700 k Ω and ~500 k Ω for moving them over a step edge. Figure 36a – c demonstrate that it is even possible to “dig out” single copper atoms from even higher coordinated sites. The single Cu atom (Figure 36a) is used as a marker. Figure 36b, c show the drag out of single Cu atoms leading to a corresponding vacancies in the initial site of the atoms.

Furthermore instead of moving single atoms, the lateral manipulation technique is also capable to move entire molecules. Gimzewski et al. deposited hexa-*tert*-butyl decacyclene (HB-DC) molecules onto a Cu(100) surface [50]. The decacyclene core of the HB-DC is equipped with six bulky *t*-butyl-legs (Figure 37). At monolayer coverage, the molecules are immobile, forming a two dimensional van der Waals crystal (Figure 38). Separated HB-DC molecules on a Cu(100) surface are extremely mobile, making it impossible to get STM images with atomic resolution.

For this reason a coverage of just less than one monolayer was chosen and STM images resemble those of the immobilized 2-D lattice at full monolayer coverage. However, there are some random voids. In this layer the molecules can be at sites with different symmetry with respect to the surrounding molecules (Figure 39). Molecules at sites of lower symmetry rotate at speeds higher than the scan rate used for imaging and therefore appear as torus Figure 40a. The molecules at the higher symmetry sites are observed as six-lobed images, proving that they are immobile Figure 40b. Gimzewski used the lateral manipulation to drag a rotating HB-DC molecule from a low symmetry site into a higher symmetry site and the six lobes of the immobilized molecule was again clearly observed.

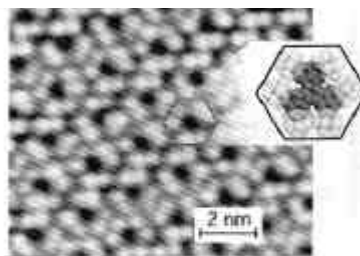
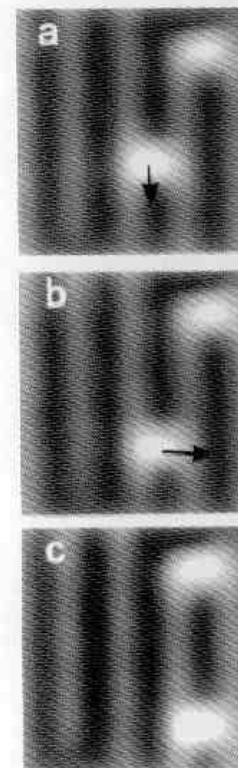


Figure 38: STM image of a Cu(100) surface after exposure to a full monolayer coverage of HB-DC molecules at room temperature. Image area is 11.4 nm by 11.4 nm [50].



Possibilità di manipolare atomi del substrato o di film molecolari

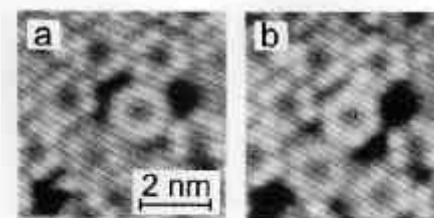


Figure 40: STM images of a Cu(100) surface after exposure to a coverage just below one complete monolayer of HB-DC molecules at room temperature. In (a) the molecule is imaged as a torus and is in a location where it is not in phase with the overall 2D molecular overlayer. The molecule is rotating. (b) The same molecule is translated by 0.26 nm and imaged as a six-lobed structure in registry with the surrounding molecules. Image area is 5.75 nm by 5.75 nm.

Manipolazione verticale

5.2 Vertical Manipulation

In the vertical manipulation process, the adparticles are transferred from the sample surface to the tip apex and vice versa [51], [52]. The first experiments on vertical STM manipulation were carried out by Eigler "picking up" Xe atoms [51]. The group of Rieder showed that transferring a Xe atom to the tip apex leads to markedly improved resolution [53]. The single Xe atom obviously "sharpens" the tip.

In Figure 41(a) [54], [55] a schematic presentation of the pick up process of a CO molecule from Cu(111) is shown. It is well known that CO molecules stand upright on a Cu(111) surface [56] with the carbon atom bonding to the copper atoms. Due to occasional contact between the tip and the surface some copper atoms are transferred to the tip apex. During the transfer of the CO molecule to the tip, the molecule must consequently rotate. A reliable procedure for transferring the CO to the tip and back to the surface requires ramping of the tunneling voltage and the simultaneous decrease of the tip-surface distance. Figure 41b and c show that scanning with a CO molecule on the tip apex leads to a clear chemical contrast. Figure 41b is scanned with a clean metal tip and all adsorbents appear as depressions. After the transfer of the CO molecule to the tip apex (indicated with a white arrow) and rescanning the area, Figure 41c shows that all CO molecules changed their appearance to protrusions. Only the oxygen atom in the upper left part of Figure 41b and c retains its appearance.

In [57] it has been described, how to combine the potential of single atom manipulation of STM and single atom sensitivity of an atom probe mass spectrum to realize an ultimate technique for surface science. The System used by Shimizu et al. consists of an STM, an atom probe, load lock chambers and a mechanism to transfer tip and sample. The tip can be transferred reversibly between the STM and the atom probe stages. To investigate the pick-up of Si atoms during manipulation, a clean Si surface was approached with a clean tungsten tip applying a bias of + 2 V and 0.3 nA at the sample. After manipulation the tip was transferred from the STM to the atom probe. The atom probe analysis showed the formation of two different layers on top of the tip apex. The top most layer was WSi_2 and the next layer was W_3Si_3 , finally the clean tungsten surface appeared. Using this combination of an STM and an atom probe could prove that the tips during manipulation do not only adsorb atoms but furthermore depending on the conditions alloys can be formed.

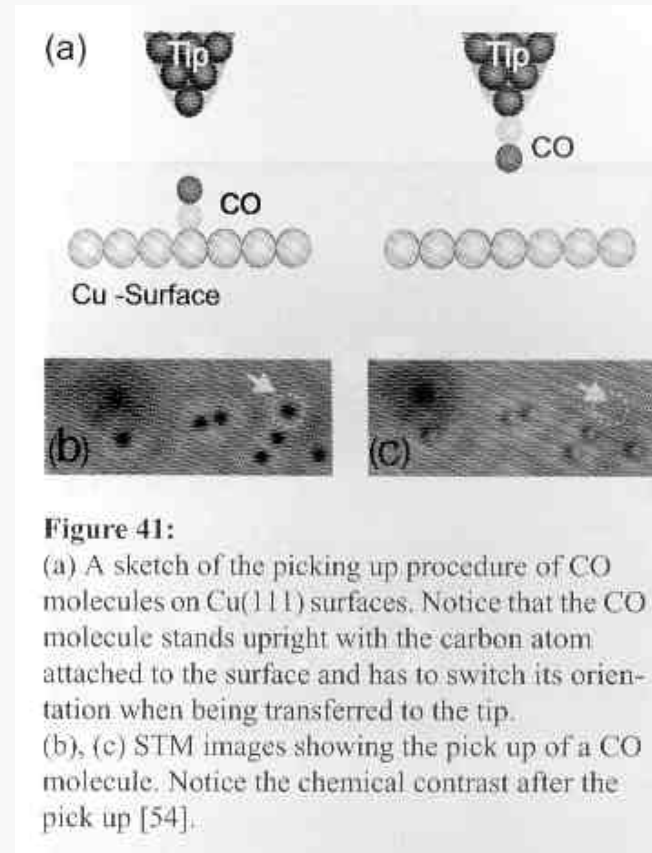


Figure 41:

(a) A sketch of the picking up procedure of CO molecules on Cu(111) surfaces. Notice that the CO molecule stands upright with the carbon atom attached to the surface and has to switch its orientation when being transferred to the tip. (b), (c) STM images showing the pick up of a CO molecule. Notice the chemical contrast after the pick up [54].

Molecole (o atomi) "sollevati" e "riappoggiati" tramite variazioni della corrente di tunneling

Nanomodificazioni con STM I

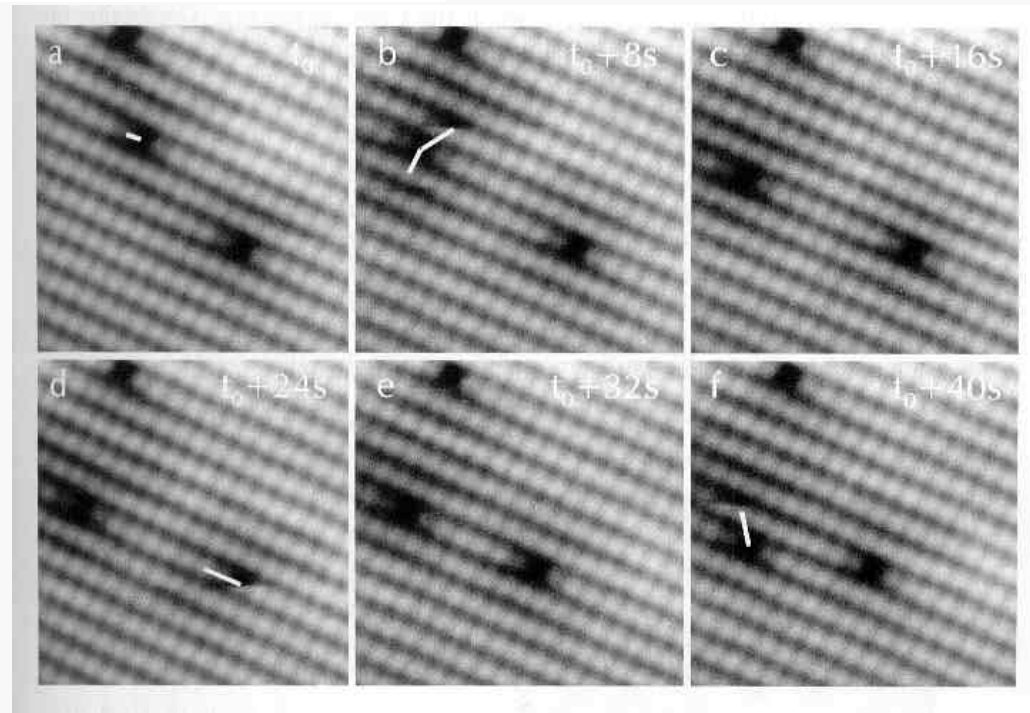
5.3 Effects induced by the Tunnel Current

It is also possible to excite atoms by the tip-sample interactions. Figure 42 shows a set of consecutive STM images acquired with 8 s time interval. The images show that the defects change their lattice positions [58], [59]. The tip can excite defects by several physical mechanism. The case shown here is based on a field-induced migration, due to the strong electrostatic field penetrating into the semiconductor. Defects can, however, also be excited by tunnelling of minority carriers into defect states followed by a charge carrier recombination with electron-phonon coupling [47]. There are surely even further mechanisms which may possibly excite atoms on the surface. Which of those will take place depends sensitively on the measurement conditions.

Finally, in Figure 43 the cutting of a carbon nano tube with an AFM is presented [60]. Earlier experiments controlling the length of carbon nano tubes were carried out using a STM [61]. At first the 600 nm² area is scanned then the AFM cantilever is lowered at the positions marked in the left image and for cutting a voltage pulse of -6 V is applied. The image on the right hand side shows the carbon nano tube after cutting.

Campo elettrico creato dalla punta "eccita" difetti la cui posizione spaziale può essere nanomanipolata

Figure 42: Migration of three phosphorus vacancies on the GaP(110) surface. The changes of the lattice positions of the vacancies is induced by the tip of the scanning tunnelling microscope. In this particular case the jumps are field-induced.



Nanomodificazioni con STM II

9.4 Nanofabrication in Solution and in Gaseous Environments

Electron-beam-induced etching and deposition is a way of writing patterns on substrates in solution and in gaseous environments. The basic idea for etching and deposition is very simple. The focused beam is used to supply energy to decompose chemicals in a localized region. The decomposition products can include a metallic species to be deposited on a surface, or a corrosive species intended to participate in an etching reaction resulting in locally etched structures on a surface. The substrates used include Si, GaAs, graphite and metals. The STM system for operation in solution should supply the necessary solution. To minimize unwanted Faradic leakage current, the tip must be treated using some special methods such as coating wax up to the extreme end of the tip (Chap.4). Deposition and etching can also be induced with the STM tip as an electrochemical electrode to drive a localized Faradic current of ions. A gaseous environment can be utilized by introducing organometallic gas with a pressure of several Pa into a vacuum chamber with a base pressure of $10^{-5} \div 10^{-6}$ Pa. For different deposition metals, the introduced gas is different. They include DMCd, $W(CO)_6$, WF_6 , and organometallic chemical of Au. Three possible mechanisms have been assumed to account for the dissociation of organometallic molecules [9.35]. (i) Electrons tunneling inelastically between the tip and sample break apart gas molecules adsorbed on the surface of the substrate. (ii) Current traveling between the tip and sample can locally heat the surface of the substrate enough to cause pyrolytic dissociation of adsorbed gas molecules. (iii) High fields between the tip and sample break down the gas creating a microscopic plasma between the tip and sample which then deposits the metal atoms on the surface. All of these will break the chemical bonds from the energy of electrons traveling between the tip and sample, thus the STM ought to be operated in the field-emission mode.

Nanomanipolazione di atomi di Xe

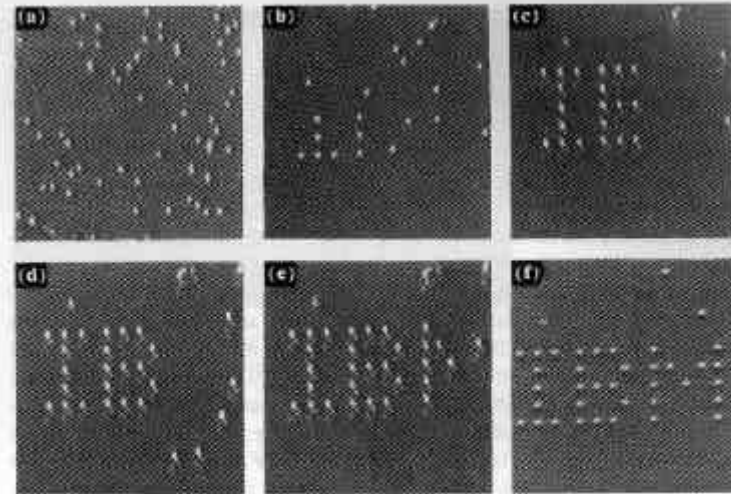


Fig. 9.10a-f. A sequence of STM images taken during the built-up of a patterned array of the letters I, B and M constructed of xenon atoms on the Ni(110) surface. The atomic structure of the nickel surface is not resolved. (a) The surface after xenon dosing. (b)-(f) Various stages during the construction. Each letter is 5 nm from top to bottom [9.40]

Campi elettrici associati con STM
(soprattutto in field-emission mode) usati
per indurre “reazioni” locali

Nanomodificazioni con STM III

5.4 Complex Chemical reactions with the STM

In 1904, Ullmann et al. heated iodobenzene with copper powder as catalyst and discovered the formation of biphenyl with high purity [62]. This aromatic ring coupling mechanism is now nearly 100 years old and known as the Ullmann reaction. Combining the presented STM manipulation methods, namely the moving of adsorbents and the influence via increased tunnel current, it is possible to control this complex chemical reactions at low temperatures step by step. S. H. Hla et al. presented the synthesis of one biphenyl molecule out of two iodobenzene on a copper surface at 20 K [48].

The synthesis consists of three different steps. First two iodobenzene (C_6H_5I) have to be dissociated into phenyl (C_6H_5) and iodine (Figure 44a and b). Secondly the two phenyl rings have to be located one to another (Figure 44d and e) and finally in the third step, through tunnelling electrons the two phenyl rings are associated to biphenyl (Figure 44e).

To abstract the iodine from the iodobenzene the STM tip is positioned right above the molecule at a fixed height and the sample voltage is switched to 1.5 V for several seconds. The energy transfer from a single electron causes the breaking of the C-I bond

Figure 45a – c, [62]. As the bond energies of the C-H and C-C bonds are two and three times higher than the C-I bond, it is not possible to break them with a single electron process at this voltage. After preparing to phenyl reactants and moving away the iodine, the left phenyl Figure 45c is brought close to the other one by lateral manipulation using the tip adsorbate forces Figure 45d. Though the two phenyls are close together they do not join at 20 K. The two phenyls can easily be separated again by lateral manipulation. Both phenyls are still bound to the Cu step edge via their σ_{C-Cu} bonds. Figure 46 shows a model where the phenyl is lying with its δ ring on the terrace while one of its C atoms is pointing towards the step edge and σ -bonding to a Cu atom. The final reaction step to associate the two phenyls to biphenyl is done by positioning the tip right above the centre of the phenyl couple and increasing the current drastically. The successful chemical association can be proved by pulling the synthesized molecule by its front end with the STM tip [62].

Reazioni
elettrochimiche
“controllate”
localmente da STM

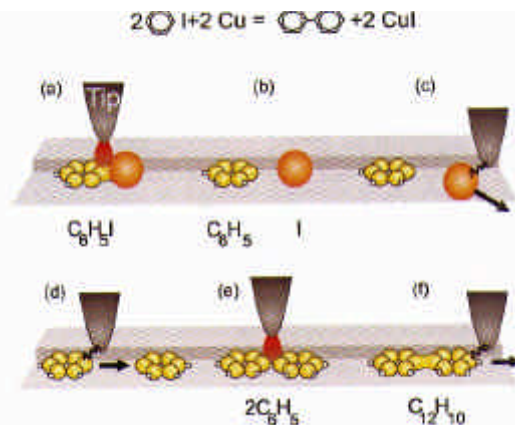


Figure 44: Schematic presentation of the tip-induced Ullmann reaction. (a), (b) Electron-induced abstraction of the iodine from the iodobenzene. (c) Pulling the iodine atom to a terrace site. (d) Bringing together to two phenyl molecules by lateral manipulation and (e) electron-induced chemical association to biphenyl. (f) Pulling the synthesized molecule by its front end to prove the association.

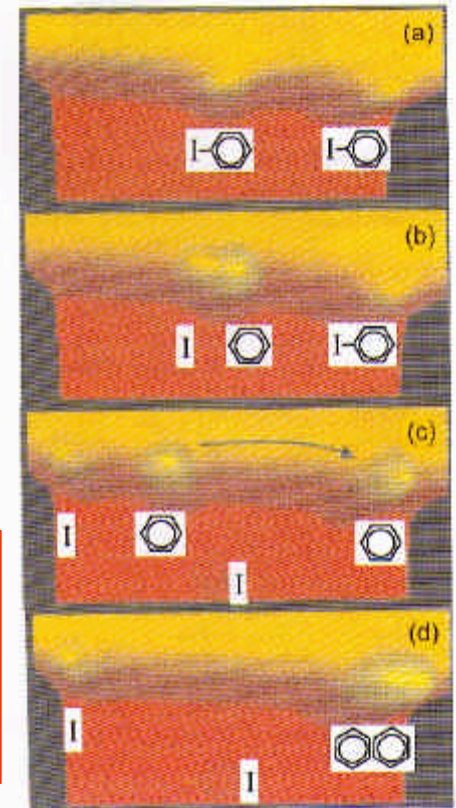


Figure 45: STM image of the Ullmann synthesis induced by the tip. (a) Two iodobenzene molecules are adsorbed at a Cu(111) step edge. Introducing a voltage pulse through the tip abstracts the iodine from the phenyl molecules. (b) (the left molecule). (c) By lateral manipulation the molecules are further separated and (d) the phenyl molecules are moved together to prepare for their association. (scan area $7 \times 5 \text{ nm}^2$) [48]

Nanolitografia su resist con STM

9.3 Nanolithography on Resist Films

Direct writing of nanometer-scale features on organic materials opens the door to using film as a resist for the etching mask and the possibility of etching in air [9.30].

The resists can directly be exposed with conventionally focused electron beams to create various structures. The e-beam resist materials frequently utilized in conventional lithography are PolyMethylMethAcrylate (PMMA) and polydiacetylene with urethane substituents (P4BCMU). They are typically sensitive to low-energy ($<20\text{eV}$) electrons. The primary beam of a conventional e-beam lithography system has a considerably higher energy, so exposure of the resist occurs through interactions with secondary and backscattered electrons produced by the primary beam; a resist is consequently exposed over an area which is significantly larger than the primary beam spot size. The STM, even working in the field-emission mode, can supply focused electron beams with low energy which can interact with resists directly. Because the tip can be held within a few nanometers from the sample, which leads to an effective beam spot size on the sample of the order of the tip-sample separation, and the tip can transversely scan over the surface controlled precisely by a computer, STM can easily be employed in lithography for writing directly on the resist surface. The degradation in resolution because of interactions between the resist material and secondary electrons in conventional lithography can be overcome in STM lithography, which makes it possible to obtain more precise structures. Using STM it is also possible to make a thorough investigation of the exposure mechanism by controlling the bias voltage precisely (i.e., the energy of electrons with which the resists are exposed) in a certain time interval under constant current. In addition, STM generally ought to work in the field-emission mode because the electrons must have enough energy to induce a chemical reaction in resists (i.e., to expose resists). In this mode, a linear

dependence of the tip-sample separation on the bias is expected in the absence of geometric effects, which make the widths of the features increase with the bias voltage.

In order to be successfully exposed with an STM, the resist film coated on conducting substrates such as Si, GaAs, Au, graphite and so on must be extremely thin, on the order of a few tens of nanometers, for two reasons. First, the low-energy electrons must be able to completely penetrate the film in order to properly expose it and to prevent excessive charging of the surface. Second, if the film thickness is greater than the gap between the tip and the conducting substrate, the tip will penetrate and damage the resist film. Experimentally, the thickest film that can be used is $V\text{ nm}$, where V is the bias voltage in volts. There are different kinds of materials which can be used as resist films in STM lithography, including polymers such as PMMA and P4BCMU which were often employed in conventional e-beam lithography, metal halides such as GaF_2 and AlF_3 , etc. The resist can be applied to the substrates by evaporation or deposited from a Langmuir-Blodgett (LB) film balance and spin coating.

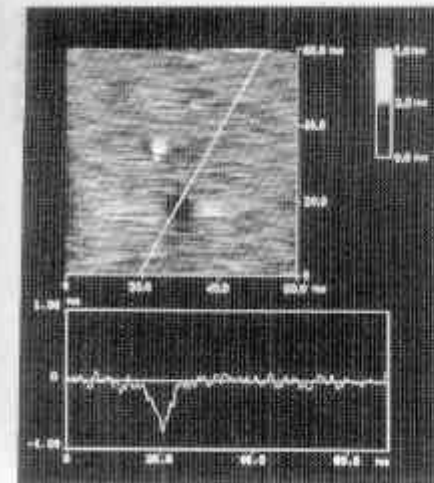


Fig. 9.3: The cross sectional profile of a STM fabricated crater on HOPG fitted with the numerical results derived from a low energy electron diffusion model [9.15]

Patterning (seriale!) di resist con STM:
vantaggi rispetto ad e-beams

“Dip pen” con AFM

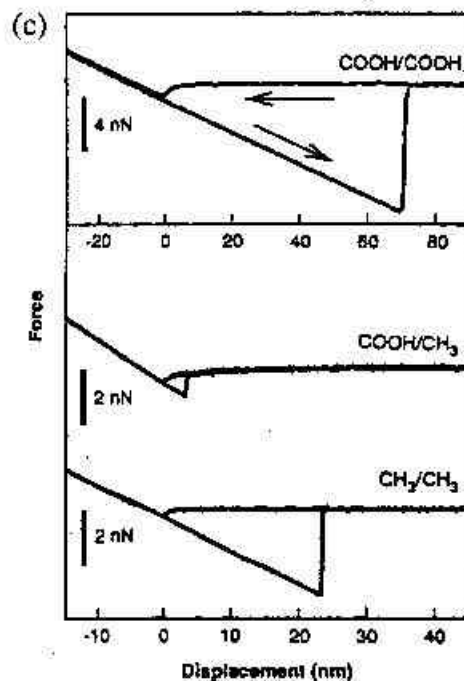
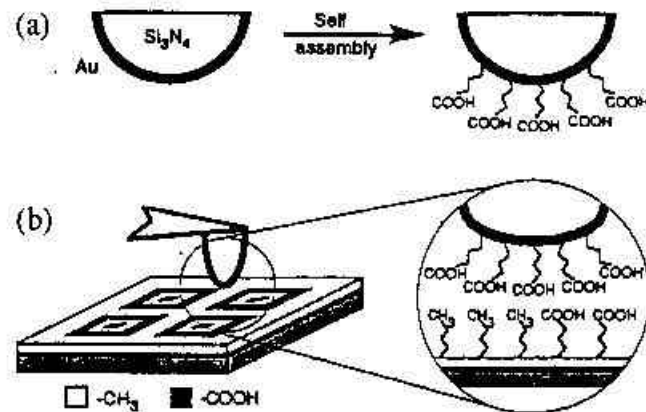


Fig. 8. 16a-c. (a) Schematic of the surface modification of the cantilever-tip assembly with a specific functional group. (b) The interactions between a tip terminating in COOH groups and a patterned sample terminating in both CH₃ and COOH groups. (c) Typical force versus displacement curves recorded between a COOH-terminated tip and sample, a CH₃-terminated tip and COOH-terminated sample, and a CH₃-terminated tip and sample in ethanol [8.62]

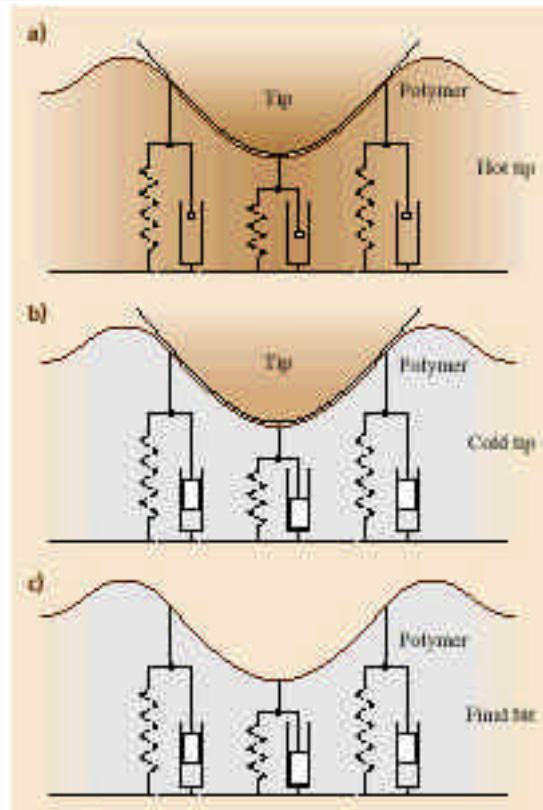
Ulteriore possibilità degli SPM:
Uso di tips funzionalizzate con gruppi
molecolari

Modificazioni superficiali (locali) di substrati
molecolari

Nanoscrittura tramite nano-funzionalizzazione

Nanoindentation I

Microscopia a sonda
(soprattutto, AFM) usata
per modifiche “plastiche” a
superfici



31.7 Polymer Medium

The polymer storage medium plays a crucial role in millipede-like thermomechanical storage systems. The thin-film multilayer structure with **PMMA** as active layer (see Fig. 31.2) is not the only possible choice, considering the almost unlimited range of polymer materials available. The ideal medium should be easily deformable for writing, yet indentations should be stable against tip wear and thermal degradation. Finally, one would also like to be able to erase and rewrite data repeatedly. In or-

Fig. 31.18a-c Viscoelastic model of indentation writing. (a) The hot tip heats a small volume of polymer material to more than Θ_g . The shear modulus of the polymer drops drastically from GPa to MPa, which in turn allows the tip to indent the polymer. In response, elastic stress (represented as compression springs) builds up in the polymer. In addition, viscous forces (represented as pistons) associated with the relaxation time for the local deformation of molecular segments limit the indentation speed. (b) At the end of the writing process, the temperature is quenched on a microsecond time scale to room temperature; The stressed configuration of the polymer is frozen-in (represented by the locked pistons). (c) The final indentation corresponds to a metastable configuration. The original unstressed flat state of the polymer can be recovered by heating the indentation volume to more than Θ_g , which unlocks the compressed springs (after [31.15]).

der to be able to address all important aspects properly, some understanding of the basic physical mechanism of thermomechanical writing and erasing is required.

31.7.1 Writing Mechanism

In a *gedanken* experiment we visualize writing of an indentation as the motion of a rigid body (the tip) in a viscous medium (the polymer melt). Let us initially assume

that the polymer, i. e., **PMMA**, behaves like a simple liquid after it has been heated above the glass-transition temperature in a small volume around the tip. As viscous drag forces must not exceed the loading force applied to the tip during indentation, we can estimate an upper bound for the viscosity ζ of the polymer melt using Stokes's equation:

$$F = 6\pi\zeta v. \quad (31.1)$$

In actual indentation formation, the tip loading force is on the order of $F = 50$ nN and the radius of curvature at the apex of the tip is typically $a = 20$ nm. Assuming a depth of the indentation of, say, $h = 50$ nm and a heat pulse of $\tau_0 = 10$ μ s duration, the mean velocity during indentation formation is on the order of $v = h/\tau_0 = 5$ mm/s. Note that thermal relaxation times are on the order of microseconds [31.20, 21] and, hence, the heating time can be equated to the time it takes to form an indentation. With these parameters we obtain $\zeta < 25$ Pa s, whereas typical values for the shear viscosity of **PMMA** are at least seven orders of magnitude larger even at temperatures well above the glass-transition point [31.39].

This apparent contradiction can be resolved by considering that polymer properties are strongly dependent on the time scale of observation. At time scales on the order of 1 ms and below, entanglement motion is in effect frozen in and the **PMMA** molecules form a relatively static network. Deformation of the **PMMA** now proceeds by means of uncorrelated deformations of short molecular segments, rather than by a flow mechanism involving the coordinated motion of entire molecular chains. The price one has to pay is that elastic stress builds up in the molecular network as a result of the deformation (the polymer is in a so-called rubbery state). On the other hand, corresponding relaxation times are orders of magnitude smaller, giving rise to an effective viscosity at millipede time scales on the order of 10 Pa s [31.39], as required by our simple argument (see (31.1)). Note that, unlike normal viscosity, this high-frequency viscosity is basically independent of the detailed molecular structure of the **PMMA**, i. e., chain length, tacticity, polydispersity, etc. In fact, we can even expect that similar high-frequency viscous properties can be found in a large class of other polymer materials, which makes thermomechanical writing a rather robust process in terms of material selection.

Deformazioni (reversibili) termoplastiche utili
per data storage (es., “millipede”)

Nanoindentation II

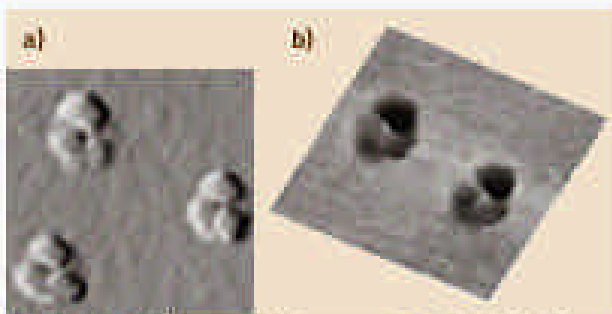


Fig. 31.20a,b Topographic image of individual indentations. (a) The region around the actual indentations clearly shows the threefold symmetry of the tip, here a three-sided pyramid. (b) The indentations themselves exhibit sharp edges, as can be seen from the inverted 3-D image. Image size is $2 \times 2 \mu\text{m}^2$ (from [31.15] © 2002 IEEE)

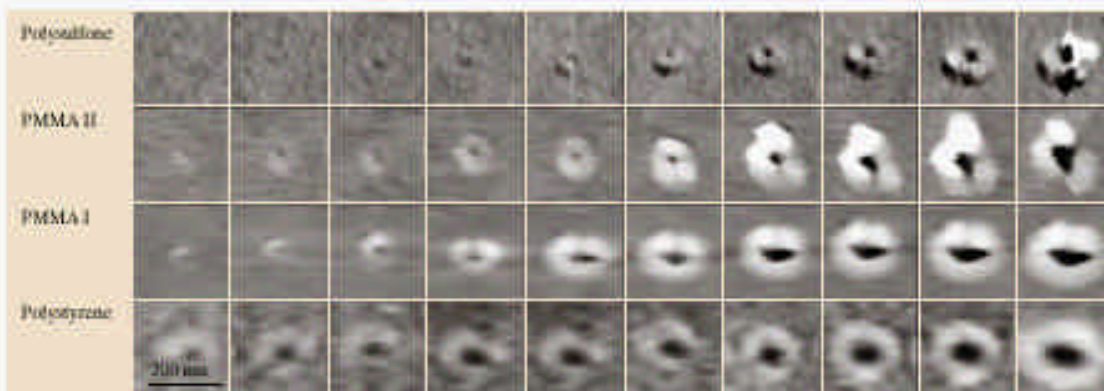


Fig. 31.21 Written indentations for different polymer materials. The heating pulse length was 10 μs , the load about 10 nN. The grey scale is the same for all images. The heater temperatures for the indentation on the left-hand side are 445, 400, 365, and 275 °C for the polymers Polyisulfone, **PMMA II** (anionically polymerized **PMMA**, $M \approx 26\text{k}$), **PMMA I** (Polymer Standard Service, Germany, $M \approx 500\text{k}$), and Polystyrene, respectively. The temperature increase between events on the horizontal axis is 14, 22, 20, and 9 °C, respectively (from [31.15] © 2002 IEEE)

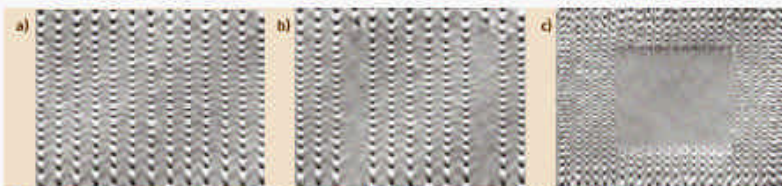


Fig. 31.25a-c Demonstration of the new erasing scheme: (a) A bit pattern recorded with variable pitch in the vertical axis (fast scan axis) and constant pitch in the horizontal direction (slow scan axis) was prepared. (b) Then two of the lines were erased by decreasing the pitch in the vertical direction by a factor of three, showing that the erasing scheme works for individual lines. One can also erase entire fields of indentations without destroying indentations at the edges of the fields. This is demonstrated in (c), where a field has been erased from an indentation field similar to the one shown in (a). The distance between the lines is 70 nm (from [31.15] © 2002 IEEE)

Possibilità di cicli termomeccanici di cancellazione e riscrittura

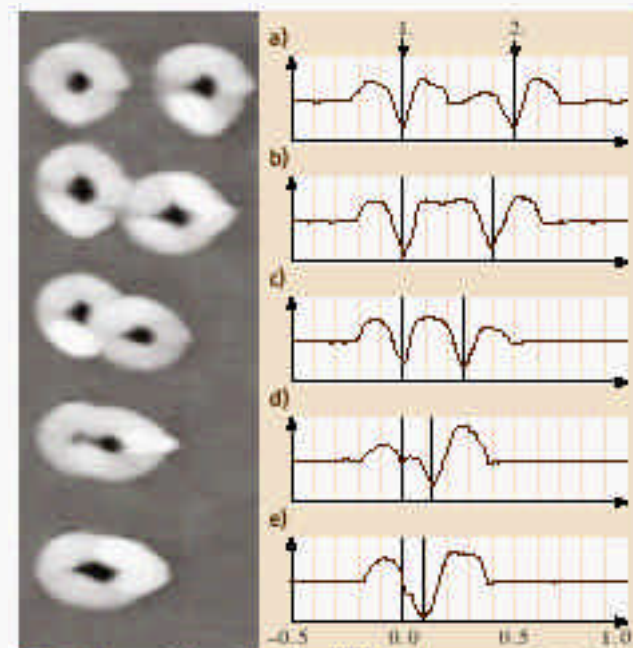
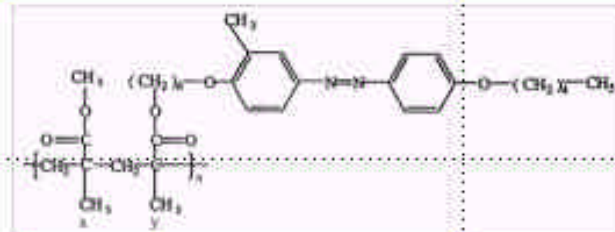


Fig. 31.24a-e Indentations in a **PMMA** film at several distances. The depth of the indentations is $\sim 15\text{ nm}$, roughly the same as the thickness of the **PMMA** layer. The indentations on the left-hand side were written first, then a second series of indentations was made with decreasing distance from the first series going from (a) to (e) (after [31.15])

Nanoscrittura con campo prossimo I

Photosensitive polymer sample

Polymethacrylate (PMA) network, modified in the four position with an azobenzene mesogenic unit (3-methyl-4'-pentyloxy) connected to the main chain by an hexamethylene spacer (PMA4).



PMA4
chemical structure
homopolymer ($x = 0$)
co-polymer ($x \neq 0$)

Samples preparation

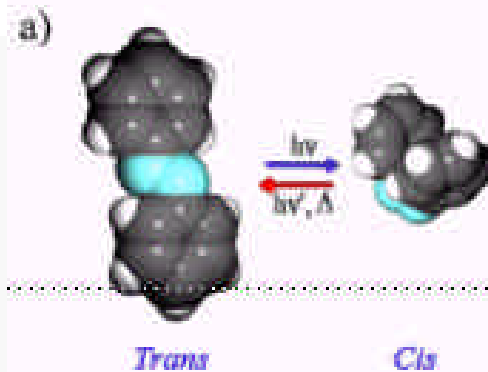
- highly concentrated solution of PMA4 powder dissolved in chlorobenzene, stirred at room temperature for a few hours
- thermal treatment before impression
- film from single drops of solution on Corning 4079 glass substrate and spinning at $\sim 2000 - 10000$ rpm.

- $T_g = 294$ K.
- Above T_g , nematic phase up to $T_c \sim 353$ K.
- Conformational transition at 320 K.
- Film thickness $\sim 100 - 200$ nm.

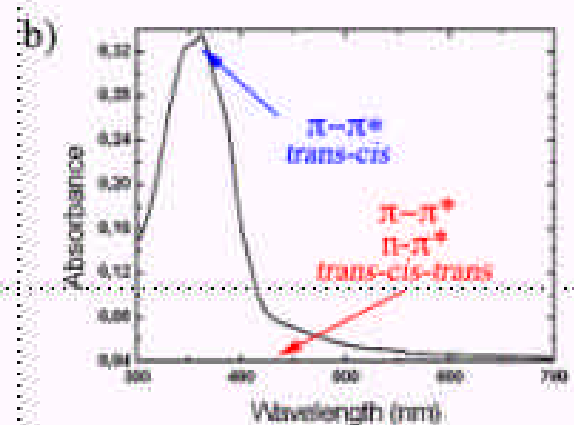
Il campo prossimo prodotto dallo SNOM può essere impiegato per provocare modificazioni (morfologiche o di proprietà fisiche) locali di materiali polimerici

Fotoisomerizzazione dell'azobenzene

See <http://www.df.unipi.it/gruppi/struttura/ma/page.htm>



Trans-cis photoisomerization of the azobenzene moiety.

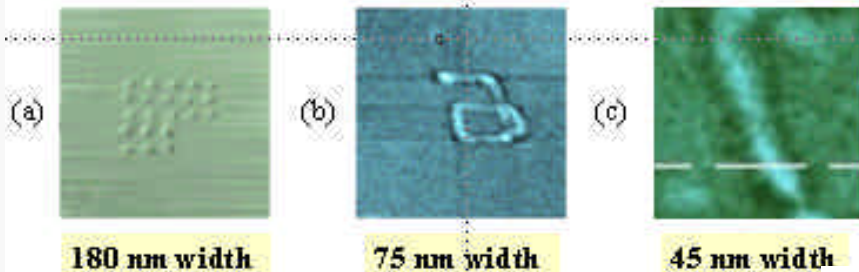


Absorption spectrum

Nanoscrittura con campo prossimo II

SNOM topography images of the optically nanostructured PMA4 thin film

- (a) homopolymer (exposure time = 1 s/dot, image size = $5 \times 5 \mu\text{m}^2$)
- (b) 30/70 copolymer (sensor speed = 20 nm/s, size = $2 \times 2 \mu\text{m}^2$)
- (c) 30/70 copolymer (speed = 50 nm/s, size = $300 \times 300 \text{ nm}^2$)

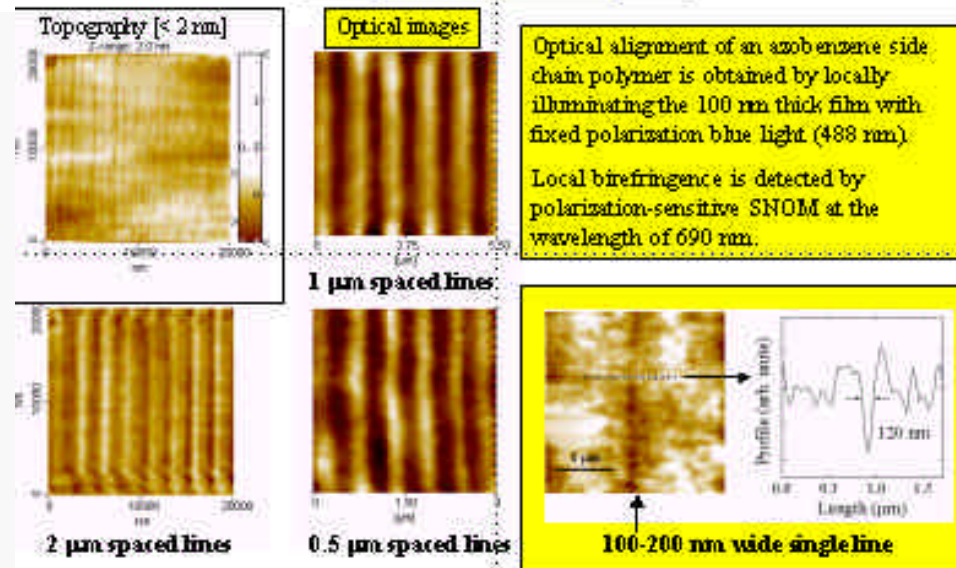


[S. Patané, A. Arena, M. Allegrini, I. Andreoni, M. Fatti, and M. Giordano, Opt Commun 210, 27 (2002)]

Nanoscrittura di strutture **ottiche** di dimensioni nanometriche tramite birifrangenza indotta (vantaggiosa in termini di tempi di risposta, non essendoci migrazione di massa)

Nanoscrittura ottica di rilievi **topografici** (per migrazione di massa o altri fenomeni morfologici superficiali)

PHOTOINDUCED BIREFRINGENCE



V. Likodimos, M. Labardi, L. Pardi, M. Allegrini, M. Giordano, A. Arena, S. Patané, APL 82, 3312 (2003)